Geomorphology and Paleoseismology of the Weinan Fault, Shaanxi, Central China, and the Source of the 1556 Huaxian Earthquake

X. Feng, J. Ma, Y. Zhou, P. England, B. Parsons, M. Rizza, R. Walker

JGR Solid Earth

RESEARCH ARTICLE
10.1029/2019JB017848

Geomorphology and Paleoseismology of the Weinan Fault, Shaanxi, Central China, and the Source of the 1556 Huaxian Earthquake

X. Feng[1], J. Ma[1,2], Y. Zhou[3,4], P. England[3], B. Parsons[3], M. A. Rizza[5], and R. T. Walker[3]

[1]Shaanxi Earthquake Agency, Xian, China, [2]State Key Laboratory of Active Tectonics and Volcanoes, Institute of Geology, China Earthquake Administration, Beijing, China, [3]Department of Earth Sciences, Oxford University, Oxford, UK, [4]Guangdong Provincial Key Laboratory of Geodynamics and Geohazards, School of Earth Sciences and Engineering, Sun Yat-sen University, Guangzhou, China, [5]Aix-Marseille Université, CNRS, IRD, CEREGE UM34, Aix en Provence, France

The 1556 CE Huaxian earthquake resulted in an estimated 830,000 deaths and caused widespread devastation in the Weihe Basin, China. Seismic intensities from historical accounts yield, via magnitude-intensity relations, a commonly quoted magnitude of 8¼ to 8½. The maximum recorded shaking was confined to a zone close to the Huashan and Weinan faults, which exhibit fresh scarps up to 7–8 m high. Recent palaeoseismic studies have suggested, however, that the Weinan fault has not ruptured at the surface for several thousand years. Furthermore, the 90-km combined length of the Huashan and Weinan faults is short for an earthquake of magnitude 8¼ to 8½. We present a detailed analysis of the Weinan fault at one well-preserved site, combining field observations and age constraints from fluvial terraces displaced by faulting, analysis of a high-resolution digital elevation model (DEM), interpretation of the walls of a quarry that cuts through the fault zone, and from a profile of borehole cores across the fault. We find that the fault ruptured within the last ~900 years and is likely, along with the Huashan segment, to be the causative fault for the 1556 earthquake. The magnitude remains uncertain, with M_w ~ 7.5 being a plausible estimate given the fault length, and no more than M_w 8.0 if we use the maximum estimates of slip. These estimates are considerably smaller than magnitudes estimated from intensities, with importance in estimating the recurrence intervals between destructive earthquakes and hazard across central China.

Key Points:
- The 1556 CE Huaxian earthquake of central China likely occurred on the Weinan-Huaxian faults
- It potentially involved slip of up to ~10 m over a length of ~90 km; its magnitude (M_w) was likely 7.5 to a maximum of 8.0
- We suggest that historical magnitude from intensities overestimates the size, with implications for seismic hazard estimates in China

Supporting Information:
- Supporting Information S1

Correspondence to:
R. T. Walker,
richard.walker@earth.ox.ac.uk

Citation:
Feng, X., Ma, J., Zhou, Y., England, P., Parsons, B., Rizza, M. A., & Walker, R. T. (2020). Geomorphology and Paleoseismology of the Weinan fault, Shaanxi, central China, and the source of the 1556 Huaxian earthquake. *Journal of Geophysical Research: Solid Earth*, *125*, e2019JB017848. https://doi.org/10.1029/2019JB017848

Received 15 APR 2019
Accepted 9 NOV 2020
Accepted article online 17 NOV 2020

1. Introduction

We examine the 23 January 1556 Huaxian earthquake in Shaanxi, central China (Figure 1a), which is the deadliest in history with an estimated death toll of ~830,000, of which roughly one third were killed by primary effects of building and cave-dwelling collapse, and of landsliding, with the remaining two thirds thought to have perished through resulting famine and disease (e.g., Hou et al., 1998; Wang, 1987; Yuan & Feng, 2010). The earthquake occurred in the basin of the river Wei (the Weihe Basin), a densely populated region that supports ~23 million inhabitants at the present day, including ~8 million in the city of Xi'an alone. In addition to its importance for the seismic hazard and risk in the Weihe Basin, this earthquake represents one of the few examples of large (magnitude greater than 7) continental normal faulting earthquakes. Such earthquakes are generally confined to regions that are deforming slowly, and in consequence, there are few opportunities to increase knowledge about the hazards posed by large normal faulting continental earthquakes in general (e.g., Doser, 1988; Hecker et al., 2010; Jackson & White, 1989; Middleton et al., 2016; Molnar & Deng, 1984).

The damaging effects of the earthquake are well known from historic records. Isoseismal contours of the Chinese seismic intensity scale are shown in Figure 1b. These isoseismals were reconstructed from primary historic sources and field surveys of historic buildings (Yuan & Feng, 2010). Strong shaking was experienced across the entire Weihe Basin, with a zone of intensity X that was ~100 km long and with intensity VIII shaking across most of the Weihe Basin. The greatest levels of shaking (XI+ to XII) were experienced in the Huaxian and Weinan regions, suggesting that the earthquake ruptured the nearby Huashan and Weinan faults (Figures 1 and 2).

Scarps up to ~8 m high along the Huashan and Weinan faults have usually been assumed to be the 1556 earthquake scarp (Du et al., 2017; Hou et al., 1998; Rao et al., 2014; Yuan & Feng, 2010; A. Zhang, et al., 1995;

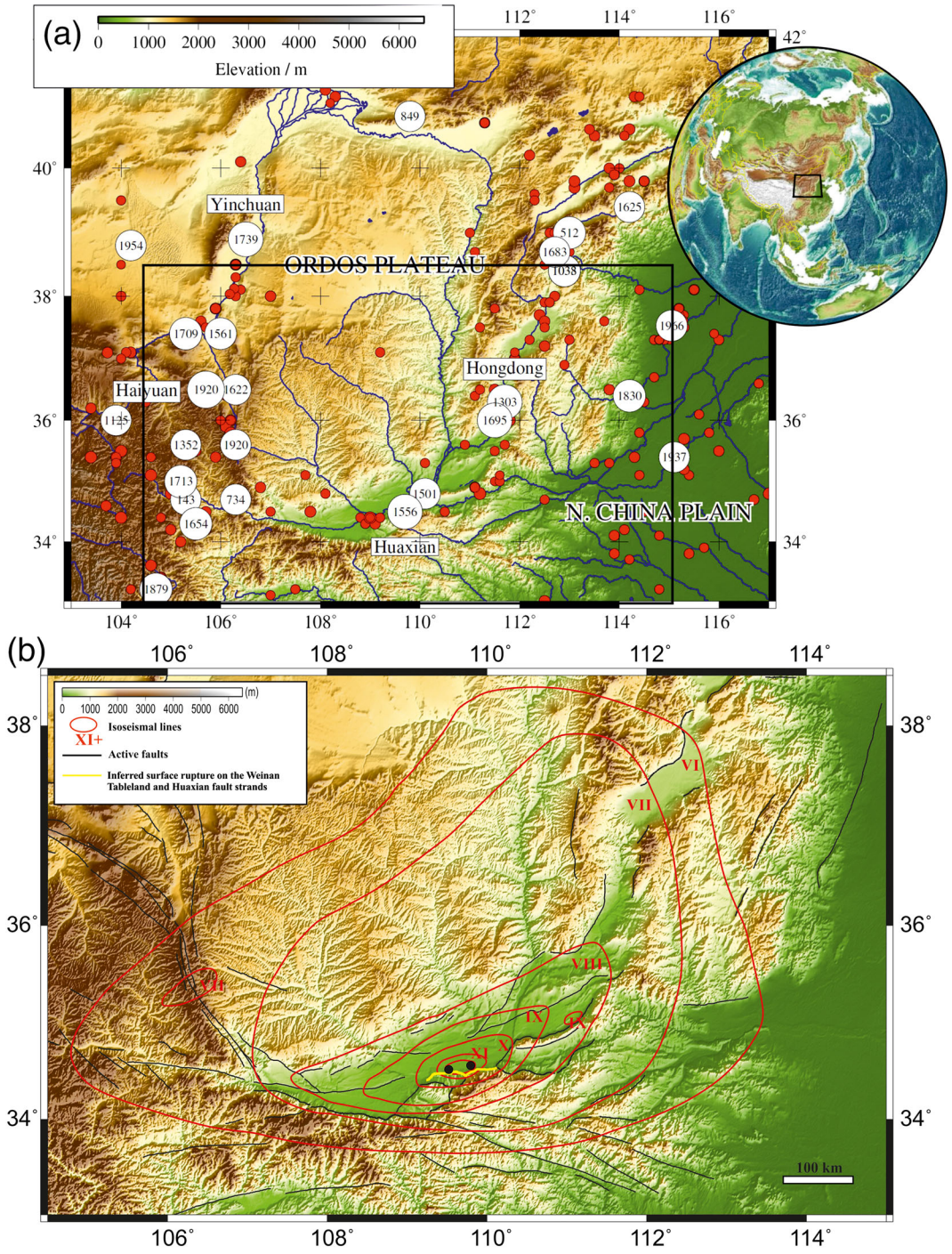

Figure 1. (a) SRTM topography (Farr & Kobrick, 2000) of the Ordos Plateau in northeastern China. Rivers are indicated in dark blue. Historical earthquakes with M_w 7 are shown by white circles, including the year in which they occurred. The 1303 Hongdong, 1556 Huaxian, 1739 Yinchuan, and 1920 Haiyuan events are labeled individually. Historical earthquakes with $M_w < 7$ are shown as red dots. Data comes from Lee et al. (1978) and Liu et al. (2011).
(b) Isoseismal map of the 1556 Huaxian earthquake. Intensity (greater than 4) was mapped by Yuan and Feng (2010) by analyzing extensive historical records and field observations. The Weinan-Huaxian area (black dots) suffered the greatest damage and is presumed to be the epicentral area. Yellow lines denote surface ruptures associated with the earthquake.

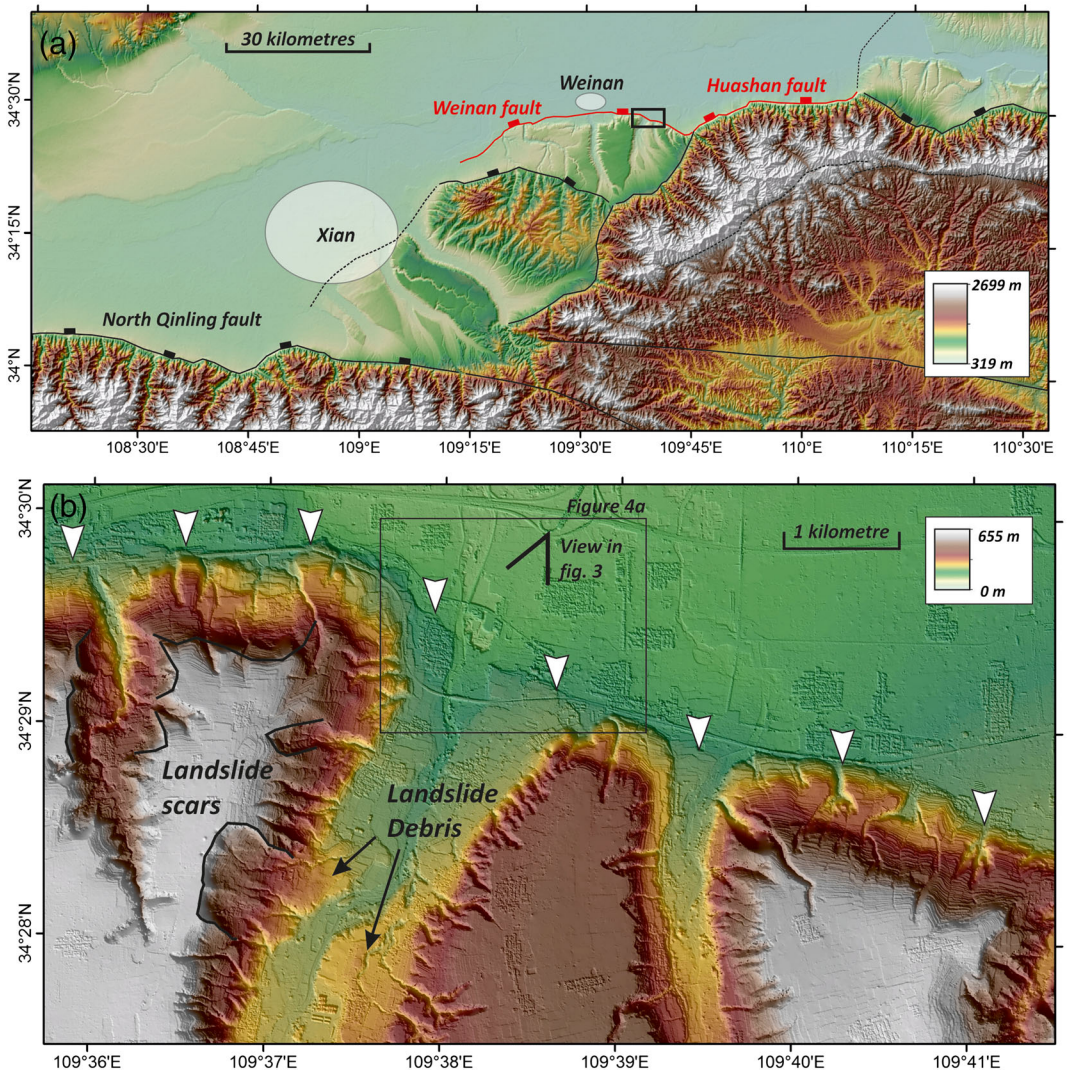

Figure 2. (a) SRTM shaded-relief topography of the eastern Weihe Graben. The Huaxian and Weinan Tableland faults are marked in red. The approximate urban area of Xian city (population ~8 million) is marked. (b) Shaded-relief Pleiades DEM with a close-up of the Chishui river catchment. White arrows indicate preserved scarps along the Weinan Tableland fault. The black box shows the region represented in Figure 4.

Y. Zhang, et al., 1998). Most of the published accounts concentrate on the scarps developed along the Huashan fault. Zhang et al. (1995) report discontinuous scarps between 3 and 8 m in height along the Huashan fault. These scarps are developed tens of meters north of the basement fault surface, and close to Huaxian town they displace a terrace containing abundant Yangshao cultural artifacts of ~4,000 years age. Hou et al. (1998) also describe the scarps along the Huashan fault, giving a range of scarp heights of ~4–7 m in the youngest generation of alluvial terrace. They date this youngest terrace at ~5,000 years based on radiocarbon dating and the presence of Longshan culture archeological material. The published information on the Weinan fault scarps is less detailed, with much of the discussion restricted to the Chishui river catchment, which also forms the focus of our present investigation. Estimates of scarp height here vary between 2–4 m (e.g., Kaizuka & Matsuda, 1992) and 7–8 m (Yuan & Feng, 2010).

As it has not so far been conclusively demonstrated that the mapped surface scarps result from the 1556 earthquake, it has led some to argue that the Weinan and Huaxian faults were not the causative faults (Hou et al., 1998; Li et al., 2015; Wang, 1980). In addition, attempts at dating sediments that bracket the most recent rupture have returned ages much older than 1556 CE, suggesting that the most recent surface rupture

was several thousand years ago (e.g., Rao et al., 2014). Also, even if the Weinan and Huaxian faults did slip in the 1556 earthquake, varying interpretations of the geomorphology of the key field sites have led to significantly different interpretations of the amount of surface slip, and of earthquake history, on the main faults (e.g., Kaizuka & Matsuda, 1992; Li et al., 2015; Rao et al., 2014; Yuan & Feng, 2010).

The magnitude of the 1556 earthquake is often stated to be 8¼ to 8½, based on a range of empirical relationships between the maximum intensity in the epicentral area and the magnitude (e.g., Yuan & Feng, 2010). The use of fractional, rather than decimal, magnitude reflects the fact that using such relationships carries an uncertainty of at least a quarter of a magnitude unit. The Huashan and Weinan faults have a combined length of ~90 km which, from empirical scaling relationships between magnitude and fault rupture length, is more consistent with a magnitude in the range ~M_w 7–7.5 (e.g., Leonard, 2010; Wells & Coppersmith, 1994; Wesnousky, 2008). The discrepancy between these estimates of magnitude could reflect inaccurate estimates of the source fault and slip in the 1556 earthquake (e.g., Li et al., 2015), but it could also be the case that the earthquake had a magnitude of less than 8 and that the intensity-magnitude relationship has led to an overestimation of the magnitude. This has recently been inferred for some other historical earthquakes within China (e.g., Kulikova & Krüger, 2017; Middleton et al., 2016; Xu et al., 2018). Ou et al. (2018) suggest that overestimates in the magnitudes of historical earthquakes in China arise due to the use of Gutenberg and Richter surface wave magnitude (M) in the conversion from seismic intensity data. In this case M 8½ will be approximately equivalent to a moment magnitude (M_w) of ~8.0 ± 0.1.

Here we attempt to resolve whether or not the scarps mapped along the Huaxian and Weinan faults represent the surface rupture of the 1556 earthquake through a detailed investigation of one site along the scarp where we are able to draw on analysis of the geomorphology, fault exposures in a quarry wall, and shallow coring of the subsurface. In our analysis we draw on the 2000 year catalog of historical earthquakes in north-central China (e.g., Liu et al., 2011), combined with the long-standing historical significance of Xian and the Weihe Basin, to assume that the 1556 earthquake is the only earthquake of equivalent magnitude to have occurred within the last two millennia. Although there is remaining uncertainty regarding whether the mapped scarps represent single event or cumulative displacements, we do find convincing evidence that they ruptured in the 1556 earthquake. We then make estimates of its maximum magnitude, based on the assumption that the scarps were formed solely by the 1556 earthquake, and we compare this value to magnitudes obtained from historical intensities. These findings are then discussed in the context of normal fault occurrence in intraplate regions and for seismic hazard assessment.

2. Geomorphology of the Chishui Catchment

Degradation of the geomorphology of the epicentral area has occurred due to widespread agriculture. Weathering and erosion present challenges for the paleoseismic investigation of the Huaxian and Weinan faults. Further modification of the landscape by recent encroachment of heavy industry has also obscured much of the longer-term geomorphology of the range fronts, leaving only a small number of sites where relatively undisturbed late Pleistocene/Holocene geomorphic markers are preserved. At some sites where rivers cross the two faults, however, a discontinuous scarp up to ~7- to 8-m height is still preserved and observed in fluvial/alluvial surfaces (Li et al., 2015; Rao et al., 2014; Yuan & Feng, 2010).

Our study focusses on the Chishui river catchment (Figures 3 and 4). This site preserves both the 7- to 8-m scarp and also higher terraces (Kaizuka & Matsuda, 1992; Li et al., 2015; Rao et al., 2014; Yuan & Feng, 2010). Using stereo Pleiades satellite data, we produce a detailed digital elevation model (DEM) of the site to examine its geomorphology. While our study was taking place the river terrace gravels were quarried (e.g., Li et al., 2015), providing an opportunity to combine our study of the surface geomorphology with interpretation of a cross section through the fault zone. The fresh exposure of sediments and structures down to a depth of ~10 m sheds light on previously reported dating results reported by Rao et al. (2014) and Li et al. (2015), which yielded widely spread ages. The high-resolution DEMs that we have produced record the geomorphology at this important site, much of which has since been destroyed by quarrying.

The Chishui study site is along the northern edge of the Weinan Tableland (Figures 2 and 3), which is a low-relief surface standing 200–300 m above the adjacent Weihe Basin. The tableland is developed in the footwall of the north dipping Weinan normal fault and is composed of exhumed and relatively soft basin deposits. These deposits were presumably laid down in the subsiding hanging wall of a fault sited further to the

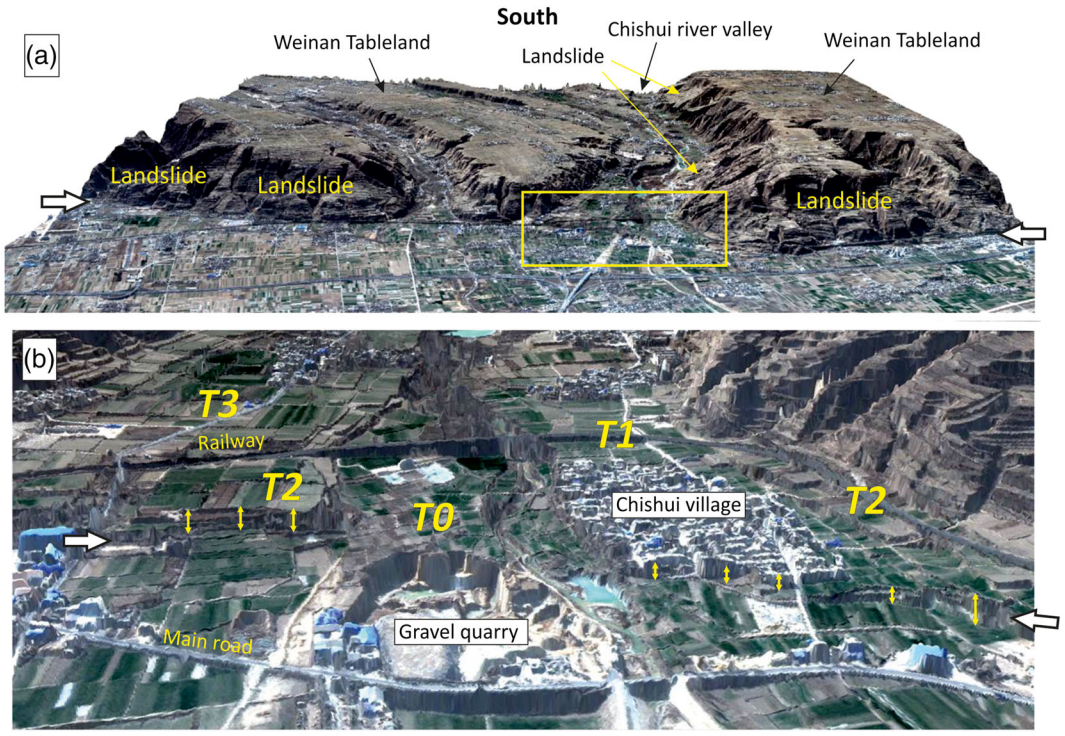

Figure 3. (a) Perspective view, looking southward, of the Weinan fault at Chishui, see Figure 2b for orientation. The fault runs along the base of the steep escarpment of the Weinan Tableland (between the white arrows). A number of prominent landslides are visible along the escarpment and also within the incised river catchments. (b) A close-up showing the geomorphology of the fault as it crosses the Chishui river terraces. The fault runs between the white arrows. Fault scarps in terrace material (T1 and T2) are marked by yellow arrows. T0 is not displaced across the fault. The gravel quarry extends to the fault in this image but was then extended southward, allowing a cross-sectional view through the fault zone.

south (Figure 2a). Uplift of the tableland with respect to the river Wei has led to deep incision of northward flowing tributaries, including the Chishui catchment, which originate in the Huashan and Qinling mountains to the south (Figure 2). The tableland surface is higher on the western side of the Chishui river than on the eastern side, suggesting that the eastern side has been eroded, likely by fluvial action, at some point in the recent geological past. Landsliding is common along the northern escarpment of the tableland and also within the incised catchments. Many, though not all, of the landslides visible in the geomorphology were likely to have been activated during the 1556 Huaxian earthquake (Yuan & Feng, 2010).

The geomorphology of the Chishui site has been described by several authors (Kaizuka & Matsuda, 1992; Rao et al., 2014; State Seismological Bureau of China, 1988) who made interpretations of the terrace stratigraphy. These interpretations differ in the numbers of past earthquake ruptures and the magnitudes of their surface displacements. To reinterpret the geomorphology of the Chishui river catchment in detail, we combined field investigation with analysis of DEM constructed from 0.5-m resolution Pleiades stereo satellite imagery (Figures 3–5). The imagery was acquired in winter, to minimize vegetation cover. Details of the imagery acquisition and processing are given in the Appendix.

A close-up of the Pleiades DEM where the Chishui river catchment crosses the Weinan fault is shown in Figure 2b and in perspective view in Figure 3. On both figures the fault is marked by white arrows. It is visible in Figure 2b as a steep scarp running from top left to lower right of the image. A patchwork of agricultural terraces covers the southern half of the image. Chishui village sits above the western bank of the river on the footwall of the fault. A collection of industrial buildings and a deep gravel quarry excavation are present in the immediate hanging wall of the fault. A prominent landslide scar and debris ~3 km south of the village is likely to relate to a landslide which occurred in 689 CE and formed a lake upstream of the fault, as described in the Historical Natural Disaster in Shaanxi Province Editorial

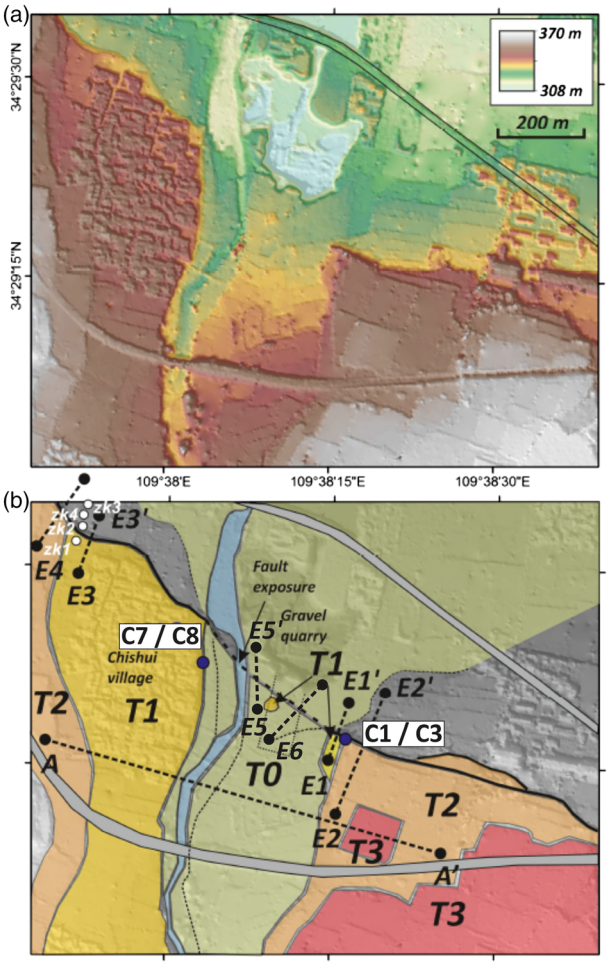

Figure 4. (a) Pleiades shaded-relief topography of the Chishui catchment. (b) Surface geomorphology of the Chishui catchment, laid over the hillshaded DEM. Footwall terraces are labeled from T0 (youngest) to T3 (oldest). A-A′, E1-E1′, E2-E2′, E3-E3′, E4-E4′, E5-E5′, and E6-E6′ are topographic profiles. "C" stands for radiocarbon samples. Dashed polygon indicates the extension of the quarry exposure. White dots are boreholes (zk1-zk4). In the absence of direct exposure we do not assign a color to the hanging wall adjacent to T1 and T2, but we consider it likely to approximate to the T1 surface.

Union (2002). "In the first year of Yongchang in Tang Dynasty (689 CE) a landslide happened at the bank of Chichi river in Huazhou with hundreds of steps sliding, which destroyed more than 130 households in one village; the river was blocked and became a lake about in depth of 100m."

We recognize four main terrace levels in the footwall of the fault (Figure 3b). Topographic profiles from the Pleiades DEM show the four river terraces and aid the interpretation of the geomorphology (Figure 5). The surface of the youngest terrace (T0) is not displaced by the fault, and its formation thus postdates the last surface slip on the fault (Figure 5, Profiles E5 and E6). The Chishui river has incised into the surface of T0 to occupy a narrow channel. This downcutting appears to have occurred in stages, as two intermediate channel positions, formed during progressive incision into the T0 surface, are preserved in the geomorphology (marked by dotted lines in Figure 4b). The ~1-m steps at the risers of these two channels inset in T0 have been interpreted by some authors as fault scarps (Kaizuka & Matsuda, 1992; Li et al., 2015). Risers marking the edges of T0 on the downthrown (northern) side of the fault are inferred from ~1-m steps in the height of the terraced land surface. South of the fault the T0 surface is farmed, and ~1 m of silty soil has developed above the fluvial gravels.

In the footwall, T0 is flanked by older terraces, T1 and T2, which are displaced by the fault, and by a higher terrace (T3), which is not preserved at the fault trace itself (Figure 4b). Chishui village sits on the surface of Terrace T1 (Figure 6a). Topographic profiles drawn across the fault, with the T1 surface in the footwall, show a scarp of ~7.5-m height at the fault (Profile E3-E3′ in Figure 5, visible in Figure 6a). Whether or not the scarp height approximates the fault throw since formation of the T1 terrace depends on whether significant deposition has occurred in the adjacent hanging wall, though for reasons described later we are confident that the scarp does reflect fault throw. T1 is best preserved on the western side of the active river channel, but small fragments may also be preserved at the eastern edge of the T0 surface (e.g., Profile E1-E1′ in Figure 5, which shows a comparable displacement to Profile E3-E3′, though with more irregular topography in both hanging wall and footwall) and as a small outlier within T0 (Figure 4b). Exposures through the T1 terrace deposits are visible directly east of Chishui village in the T0-T1 riser, which has been refreshed for the digging of an irrigation channel (Figure 6b). At this location, the exposed stratigraphy is composed of ~3 m of silty soil with occasional rounded clasts. The soil overlies fluvial gravels. Detrital charcoals that we collected from the base of the soil (HX13-C7 and HX13-C8, Table 1) yield calibrated ages of 389–206 and 392–209 cal BCE. The surface of T1 is ~5.5 m above the surface of T0 (Profile A-A′ in Figure 5).

Terrace T2 is best preserved along the eastern side of the Chishui valley where it forms an ~13- to 14-m scarp at the fault (Figure 6c; Profile E2-E2′ in Figure 5), though small parts of it are also preserved on the western bank (Profile E4-E4′ in Figure 5). We found exposures through the T2 deposits in excavations made for an irrigation canal (Figure 6d). Fluvial gravels are covered by an ~5-m-thick silty soil (Figure 6d). Near the base of the soil, we found a cultural layer containing bone and ceramic objects (Figure 6d, inset) typical of the Banpo culture (~5–8 ka; e.g., Yanping, 2013). The cultural objects were mixed with abundant detrital charcoal, of which two of our samples (HX13-C1 and HX13-C3, Table 1) were analyzed and yielded ages of 3988–3803 and 3953–3785 cal BCE. Rao et al. (2014) also appear to have visited this exposure, though they do not specify exact location, and obtained a single calibrated age of 5300 ± 30 years cal BP from organic-rich soil that they state was within the alluvial layers and so apparently out of stratigraphic order with our own two dates.

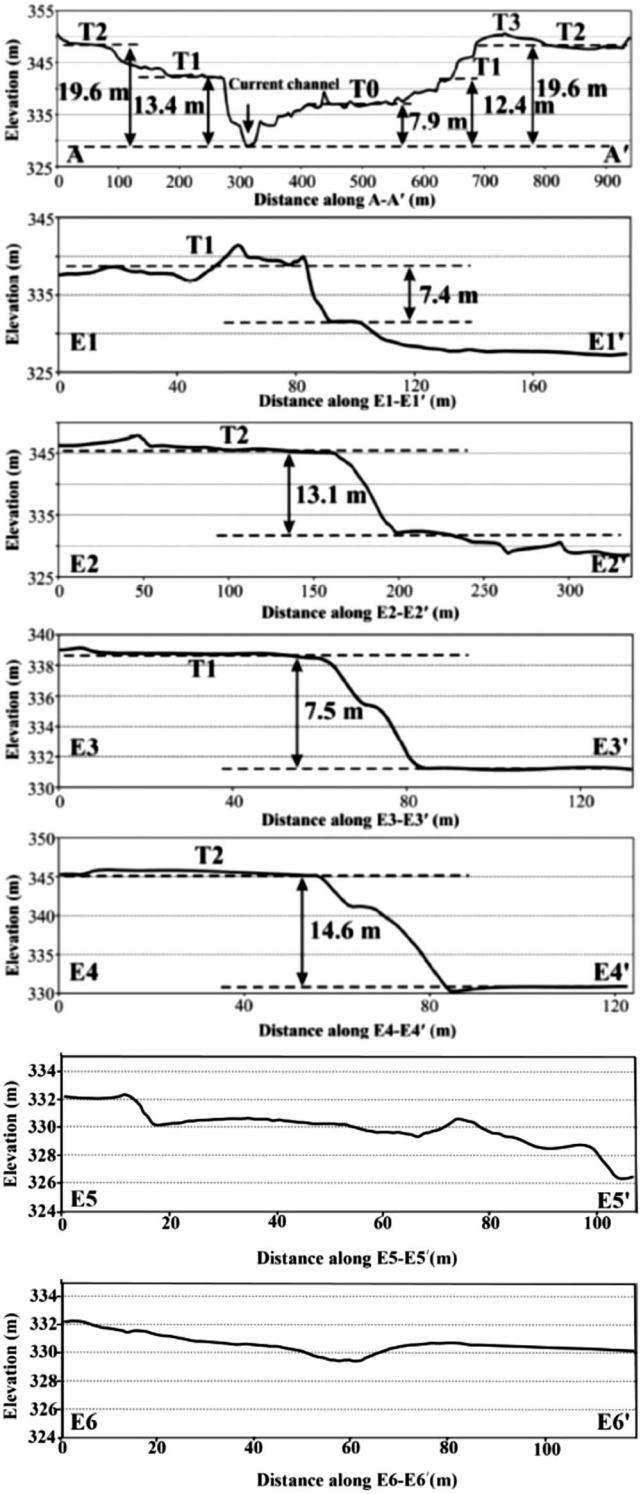

Figure 5. Topographic profiles showing river terraces and scarp heights. See Figure 4b for locations.

There are no remnants of Terrace T3 at the fault scarp. It is ~1–2 m higher than T2 and occurs only as two fragments (Figure 4b). The riser between T2 and T3 has been heavily modified for agricultural use, but the distribution of the two terraces, and the relatively small height change between them, suggests to us that they represent a system of channels within a wide river bed, similar to the nontectonic incision of the T0 surface, rather than representing two discrete periods of incision caused by faulting.

In the hanging wall of the fault the terracing is not well defined. T0 and its inset channels are visible and marked in green in Figure 4b. The hanging wall adjacent to T1 and T2, at the eastern and western sides of the study area, are not differentiated in Figure 4b. We assume, given that they are sited far from the main deposition of the Chishui river, in which only ~ 2–4 m of postearthquake gravel has been deposited in the hanging wall, that they approximate to the T1 and T2 terrace levels on the footwall. However, given that we have no exposures through them, we cannot exclude the possibility that a significant amount of sediment has aggraded since the abandonment of those terraces, such that their correlative surfaces are buried in the hanging wall.

3. Quarry Exposure

In early 2014, after acquisition of the Pleiades data the gravel quarry, the location of which is shown in Figures 3 and 4, was extended southward across the fault and through the footwall in the T0 (postearthquake) surface (also see Li et al., 2015). We constructed a 3-D model of the quarry exposure (110 m × 30 m × 11 m) from 287 field photographs using the Structure from Motion (SfM) technique (e.g., Johnson et al., 2014; Mackenzie et al., 2016; Westoby et al., 2012). Four GPS measurements were collected in the trench and used as ground control points to estimate absolute positions and scale. The 3-D model is shown in supporting information Figure S1. Ortho-rectified photo mosaics of the eastern and western walls were produced (Figure 7). The photo mosaics contain numerous artifacts introduced by uneven contrast between images. Detailed stratigraphic and structural interpretations were thus made from individual photographs and then transferred to the mosaics. Uninterpreted photo mosaics are included as supporting information Figure S2. Note that the observations and interpretations of Li et al. (2015) were made after the quarry was widened in the hanging wall, such that the hanging wall exposures that they describe are located east and west of the quarry walls as we saw them. Comparison of our own observations with those of Li et al. (2015) hence allows us to make inferences about the three-dimensional stratigraphy and structure. The units in Figure 7 are labeled from 1 (oldest) to 11 (youngest) and are correlated between the eastern and western walls, with a "w" and "e" appended to distinguish the interpretations from the western and eastern walls, respectively. Units have been divided on the basis of changes in color, dominant grain size, and sedimentary structure. Photographs of the fault zone in the western and eastern quarry walls are provided in Figures 8 and 9, along with interpretations of the detailed stratigraphy and structure.

The quarry extension exposed a main north dipping fault plane, along with the upper ~10 m of the footwall and hanging wall stratigraphy (Figure 7). The fault dips 45–55°N, and striations indicate normal faulting, with a slight left-lateral component (Li et al., 2015; Rao et al., 2014). The stratigraphy and fault zone morphology vary between the western and eastern walls, which are ~30 m apart. On each wall the hanging

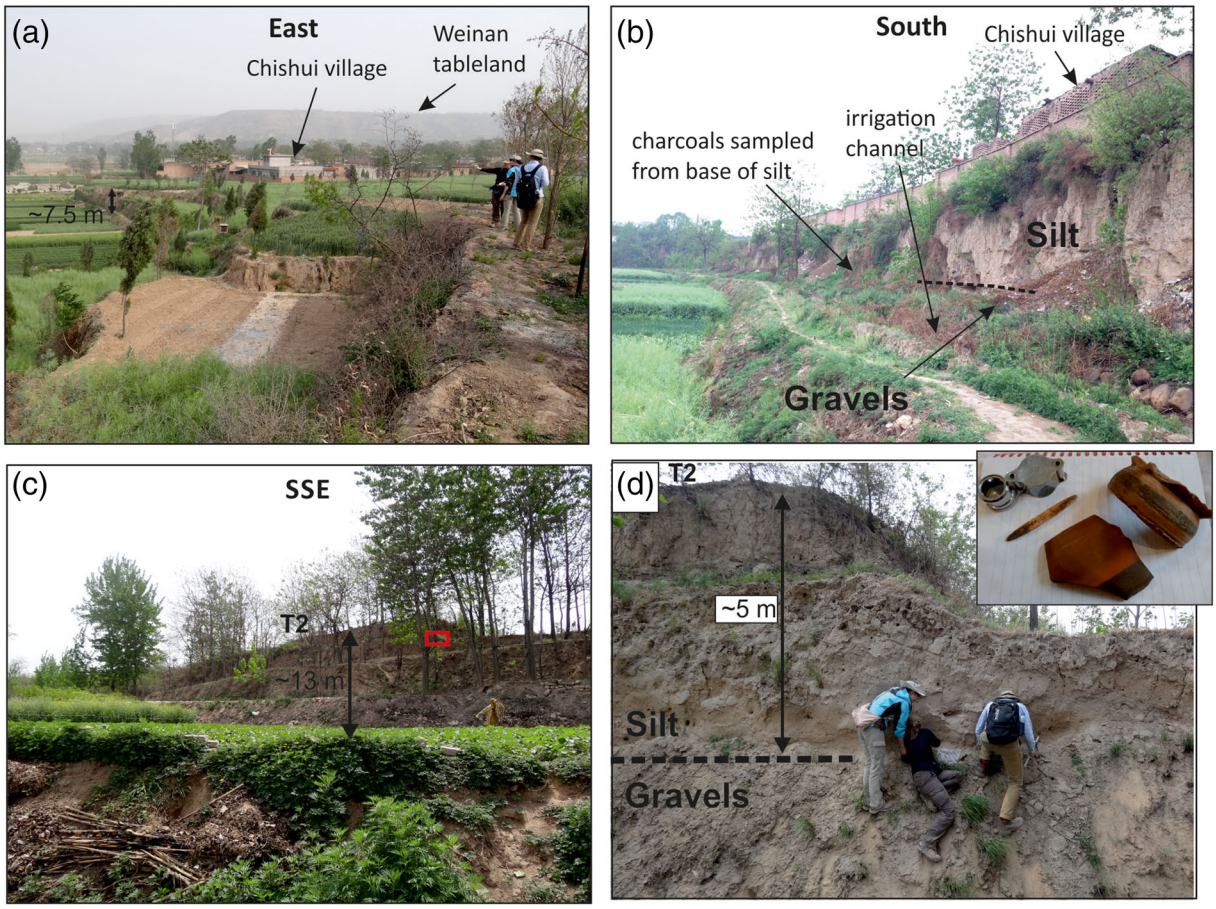

Figure 6. Field photographs (a) view eastward across the Chishui river valley. The village is built on the T1 terrace. The ~7.5-m-high scarp in T1 is marked. The elevated low-relief Weinan Tableland is visible in the far distance. The Weinan Tableland fault follows the base of the steep escarpment along the northern edge of the tableland. (b) Exposure of sediments beneath the T1 surface, beneath the village. Gravels are exposed beneath ~3 m of silt. (c) View SSE looking toward the ~13-m-high scarp in the T2 terrace. The site where we found charcoal and cultural objects is shown by the red box. (d) Sampling from the base of silt deposits beneath the T2 surface. The approximate contact between silt and underlying gravel is marked by a dashed line. There is ~5-m thickness of silt. The inset shows cultural objects typical of the Banpo culture from the exposure.

Table 1
Radiocarbon Ages of Samples

Sample	Lab number	Sample material	Locality	Measured age	Calibrated age (cal CE/BCE)
CGC-4	Beta-392747	Charred material	East Wall of Trench	880 ± 30	1042–1222 cal CE
CGC-2	Beta-387331	Organic clay	East wall of Trench	9650 ± 30	9235–8850 cal BCE
CGC-7	Beta-396733	Organic clay	East wall of Trench	2430 ± 30	750–405 cal BCE
Weinan-4	Beta-381225	Charcoal	East wall of Trench	2920 ± 30	1211–1020 cal BCE
Weinan-3	Beta-381224	Charcoal	East wall of Trench	5860 ± 30	4800–4619 cal BCE
CGC-6	Beta-396732	Organic clay	West wall of Trench	3480 ± 30	1888–1697 cal BCE
CGC-5	Beta-396731	Organic clay	West wall of Trench	2680 ± 30	897–802 cal BCE
CGC-1	Beta-387330	Organic clay	West wall of Trench	7260 ± 30	6215–6060 cal BCE
CGC-3	Beta-387332	Charcoal	West wall of Trench	1030 ± 30	901–1116 cal CE
CGC-8	Beta-399728	Organic sediment	West wall of Trench	7320 ± 30	6235–6084 cal BCE
Weinan-2	Beta-376664	Organic clay	West wall of Trench	5980 ± 30	4946–4787 cal BCE
HX13-C1	OxA-28025	Charcoal	Terrace 2	5127 ± 31	3988–3803 cal BCE
HX13-C3	OxA-28026	Charcoal	Terrace 2	5056 ± 30	3953–3785 cal BCE
HX13-C7	OxA-28027	Charcoal	Terrace 1	2240 ± 27	389–206 cal BCE
HX13-C8	OxA-28028	Charcoal	Terrace 1	2250 ± 26	392–209 cal BCE

Note. Calibration using Oxcal 4.3 with IntCal13 calibration. Calibrated ages given at 95.4% probability level. The ages with Lab number "Beta-xx" are from Beta Analytic Inc, and those with "OxA-xx" are from the Research Laboratory for Archaeology and the History of Art in the University of Oxford.

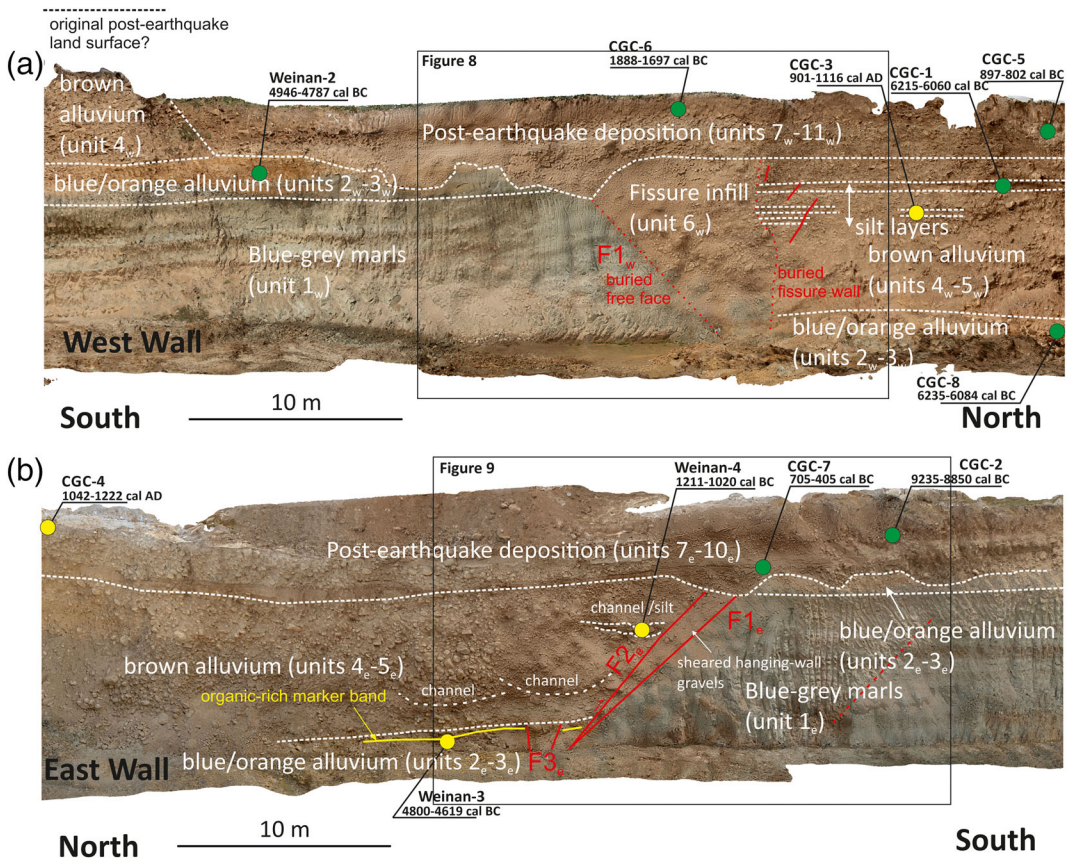

Figure 7. Orthophoto mosaics of (a) the western and (b) eastern trench walls. Horizontal and vertical scales are the same. Radiocarbon sample locations and ages are shown. Sample locations marked by yellow dots represent detrital charcoals, and green represents bulk sediment samples. The important features of the palaeoseismic interpretation are annotated (see Figures 8 and 9 for detailed logs of the fault zone). Unannotated orthophoto mosaics are included as supporting information Figure 2.

wall stratigraphy is composed of coarse river gravels, with occasional thin (10–20 cm) discontinuous bands of finer material. The footwall stratigraphy is composed of lacustrine muds and silts overlain by ~3 m of fluvial gravels. Boreholes in the basin interior have encountered similar lacustrine sediments of Pleistocene age at depths of ~150 m (Dai & Feng, 2004). Li et al. (2015) describe the footwall deposits as belonging to the Pliocene to lower Pleistocene Sanmen formation. The top of the lacustrine sediments exposed in the trench has been eroded, channelized, and unconformably overlain by the coarse gravels. Fluvial erosion of the uppermost parts of footwall and hanging wall stratigraphy, and subsequent unconformable deposition of these young gravel deposits, means that some ambiguity remains in terms of the detailed palaeoseismic interpretations. We obtained radiocarbon dates from detrital charcoal, represented by yellow circles in Figure 7, and from bulk organic-rich sediment, represented by green circles. All age data are presented in Table 1. In the following sections we document footwall and hanging wall stratigraphy and describe the observed deformation.

4. Stratigraphy

In the interpretation of the quarry walls (Figure 7) we subdivide the stratigraphy into its main components, with units numbered from 1 as the oldest. The majority of the units are correlated between the western and eastern walls and keep the unit numbering consistent between them. Subscripts of “w” and “e” are appended to descriptions from the western and eastern walls. Detailed subdivisions of the stratigraphy close to the fault zone are presented in Figures 8 and 9.

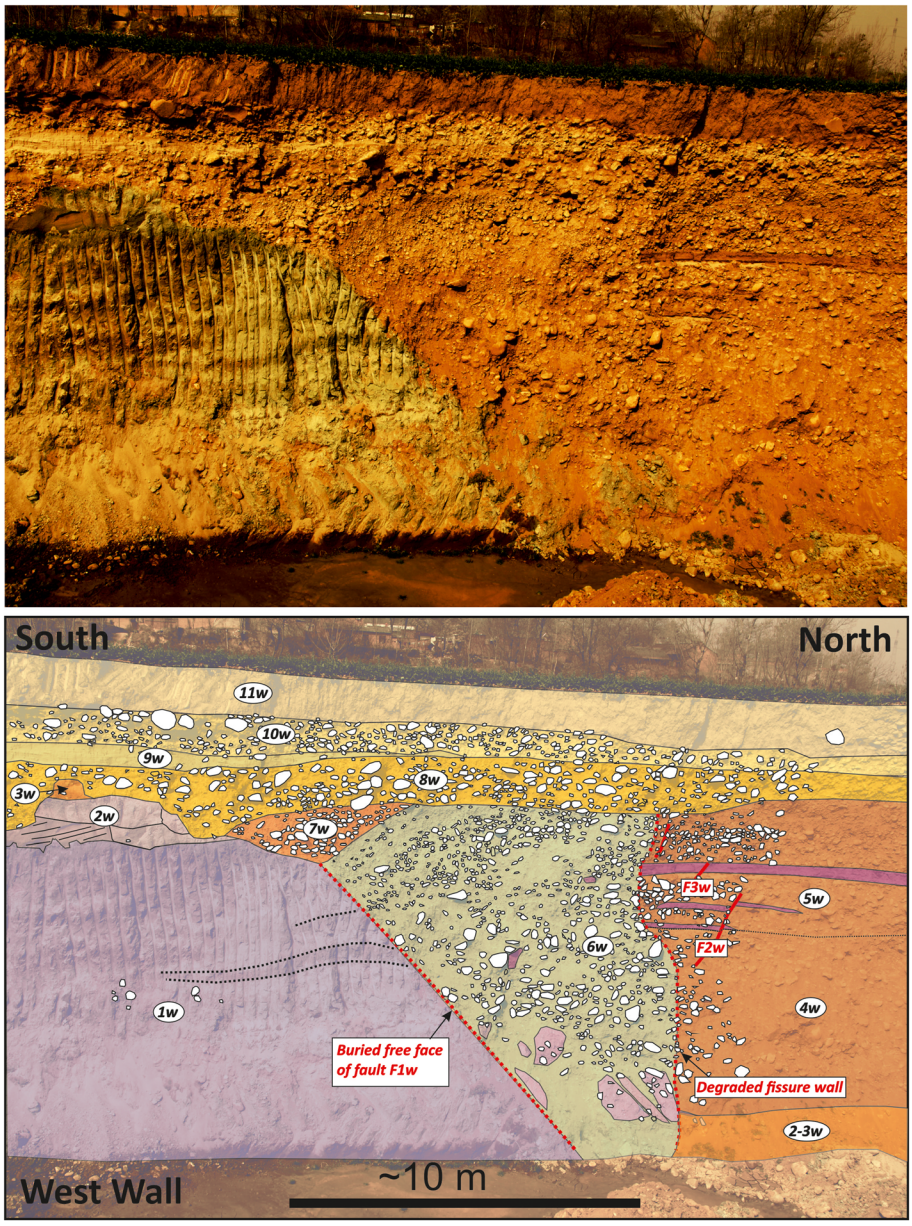

Figure 8. Interpretation of the western trench wall at the Chishui site. (top) Original photograph. (bottom) Trench log. The fault surface F1w was exhumed as a free face and then buried by fissure infill (6w). This buried free face and the degraded fissure wall to the north are shown as dotted red lines. White filled polygons are gravel clasts.

4.1. Western Wall

We interpret a buried free face encountered in the western wall ($F1_w$, Figure 7) as a fault surface that was exhumed during slip and subsequently buried. The buried fault surface dips 45°N and separates Pleistocene lacustrine deposits in its footwall from a postfaulting infill of Holocene gravels. The footwall of $F1_w$ is made up of ~6 m of banded blue-gray muds and silts (Unit 1_w, Figure 8). We interpret these deposits to have formed within a predominantly lacustrine environment, either due to localized ponding or at a time of lake formation within the main Weihe Basin. Similar deposits of early Pleistocene age are found at depths of ~150 m in the Weihe Basin (Dai & Feng, 2004) though we cannot confirm whether the exposed muds are of similar age. The muds are overlain by a channelized coarse sand to coarse gravel unit (Unit 2_w) that has a distinct blue-gray color from the reworking and incorporation of the underlying lacustrine sediment within

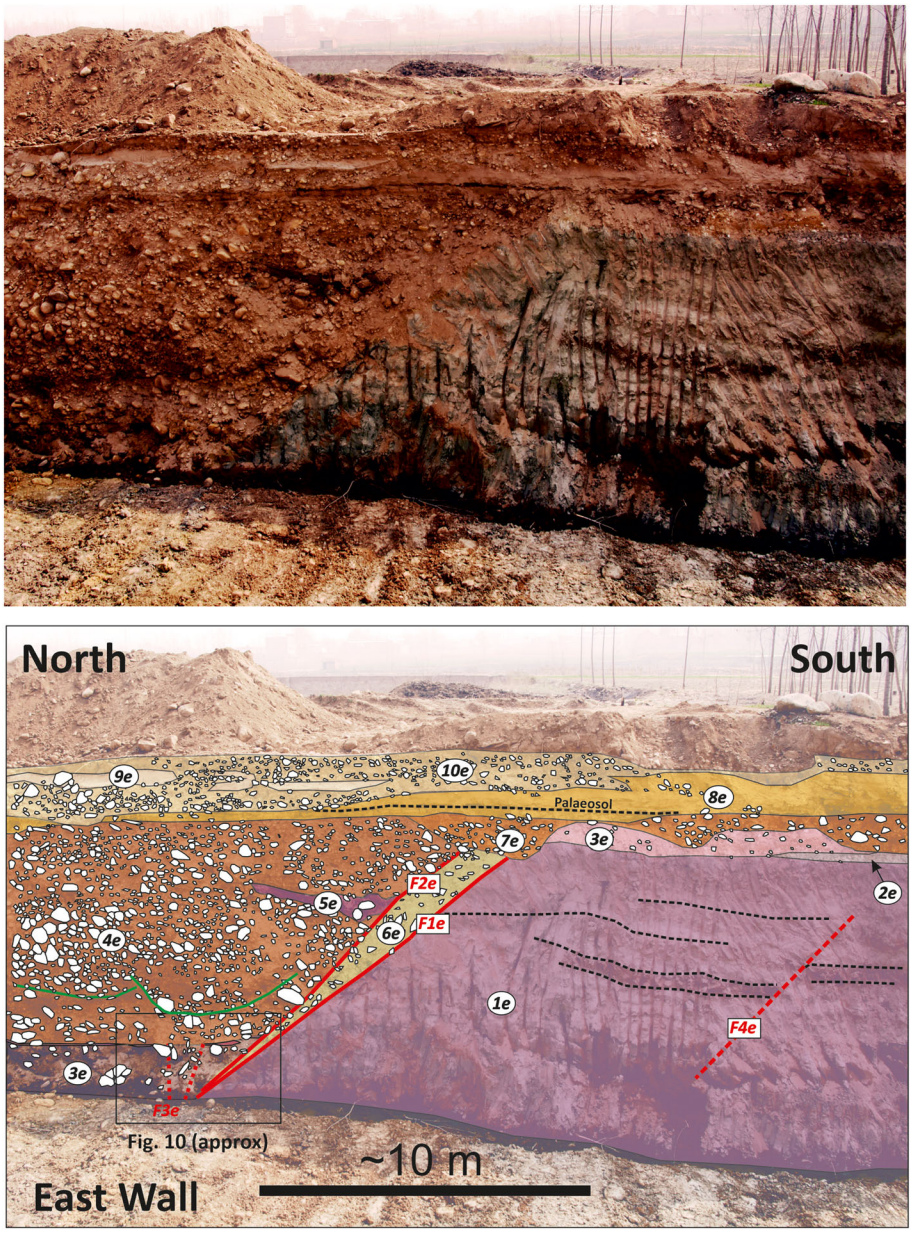

Figure 9. Interpretation of the eastern trench wall at the Chishui site. (top) Original photograph. (bottom) Trench log. F1e and F2e (solid red lines) are the main faults. F3e is interpreted to be due to the penultimate earthquake (see Figure 10 for closeup). White filled polygons are gravel clasts. Solid black line is a layer of organic-rich muds.

its matrix. The blue-gray fluvial units are in turn overlain by ~1-m thickness of dark orange gravel, Unit 3_w, (Figure 7). Clasts within the upper part of the orange gravels are coated with an organic-rich black mud.

The hanging wall sequence (right-hand side of Figure 7a) is predominantly gravel. The quarry floor likely represents the top of the blue/gray muds (Unit 1_w). The lowermost parts of the exposure are blue/orange gravels of Unit $2_w/3_w$. Above the orange gravels there is a brown gravel Unit 4_w, which is ~3 m thick, relatively poorly sorted, and with little internal sedimentary structure visible. Unit 5_w is a sequence of fluvial gravels and silts, with layering picked out within the relatively well-sorted gravels by variations in the clast size. The intact hanging wall sequence is truncated at what we interpret to be a buried free face representing a degraded fissure wall. The upper part of the wall overhangs the lower part, suggesting that the silt beds

were more resistant to degradation than the deeper parts of the hanging wall stratigraphy. The silt beds are displaced by minor south dipping faults ($F2_w$ and $F3_w$, as marked in Figure 8).

The western quarry wall cuts through a small flat-topped mound (~10 m long, 2–3 m high) within the present-day agricultural fields that we have interpreted as a small remnant of Terrace T1 that has now been eroded down, such that its surface is lower than the more extensive remnants of T1 (c.f. Figure 4, where we have labeled it as T1). The cross section through the mound exposes ~3-m thickness of coarse brown fluvial gravels, with no discernible layering, which we interpret as a fragment of Unit 4_w in the footwall, which is otherwise eroded, though well preserved in the hanging wall (Figure 7). Younger gravel units (Units 7_w-11_w) onlap against the brown gravels (Unit 4_w) and incise into the older gravel Unit 2_w. These younger deposits that overlie Unit 4_w are not deformed by faulting, and we assume that they represent postearthquake incision of the uplifted footwall, followed by aggradation of sediment within the river basin. There is no discernible thickening of these youngest deposits within the hanging wall. Before describing the postearthquake units, we first discuss the stratigraphy of the hanging wall and within the fault zone itself.

The buried free face of Fault $F1_w$ and the fissure wall define a zone filled with gravels (Unit 6_w) that widens from ~3 m at the bottom of the exposure to around 10 m at the top. The infilling gravels include coherent blocks of blue gravels mixed with brown and orange gravel clasts in its lower parts and also some fines. We consider it likely that Unit 6_w represents infill of an ~5-m-wide fissure. The blocks of blue gravel suggest that at least some of the sediment is sourced from the immediate footwall, where these units are exposed, though the degraded free face on the northern side of the fissure indicates the sediment infill was also sourced from the hanging wall. Dips of ~30°S that are observed within the upper parts of Unit 6_w suggest that these upper parts of the sediment infill were also sourced from the exposed free face on the north side of the fissure (Figure 8). Li et al. (2015) interpret the southward dip of these deposits as resulting from postearthquake deposition as a colluvial wedge, rather than colluvial fissure fill as we interpret it, though it is important to note that their observations were made after the quarry walls had been widened and the details of the sedimentary relationships obscured. We do not see strong indications that the fissure fill material has been sheared and faulted, but we cannot rule out this possibility.

The first basal unit of the postearthquake sequence is Unit 7_w, which is a coarse boulder deposit occupying a broad channel above the tip of Fault $F1_w$. It is recognizable as a distinct unit due to the uniform light-colored coating on the boulders and due to the angular unformformity with underlying units within the fault zone. Unit 7_w has in turn been channelized and infilled by Unit 8_w, which covers both the hanging wall and footwall sequence. This base of this unit defines steep-sided incisions into the footwall stratigraphy but has a smooth base above the fault zone and hanging wall sequences. Unit 9_w is a white fine-grained deposit, and Unit 10_w is composed largely of coarse boulders. The transition from silt/sand (Unit 9_w) to coarse gravel (Units 8_w and 10_w) probably represents times of active channel migration. A light brown soil (Unit 11_w) of ~1-m thickness covers the uppermost gravel layer. The present-day land surface is used for maize farming.

4.2. Eastern Wall Stratigraphy and Structure

$F1_e$ and $F2_e$ are the two main faults in the eastern wall, which together define a zone of sheared hanging wall material (Figure 7, lower panel). The ~1-m-wide fault zone, with numerous rotated clasts, separates the Pleistocene lacustrine deposits (Unit 1_e) from Holocene gravels (Unit 4_e). South of $F1_e$, the middle part of the footwall sequence, is faulted by a 50°N dipping fault ($F4_e$), with displacements of ~40 cm visible due to the offset of thin blue-gray silt beds.

The footwall stratigraphy exposed in the eastern wall is similar to that in the western wall, and we use the same unit numbering where equivalents are exposed on both walls. The banded blue-gray muds and silts (Unit 1_e) are overlain by ~1-m thickness of a blue-gray fluvial unit (Unit 2_e) and orange gravel (Unit $3_{e)}$. Unit 3_e has been incised and infilled by a unit of fluvial gravels and silts (Unit 7_e) that are part of the postearthquake sequence.

In the hanging wall the gravel Units 3_e, 4_e, and 5_e have a combined thickness of ~8 m (north of Fault $F2_e$, left-hand side of the log, Figure 7). All units have been deformed by drag in the closest meter to the main fault zone. The basal layer exposed in the hanging wall sequence is Unit 3_e, equivalent to the orange gravels described on the western quarry wall. A distinctive thin layer of organic-rich black mud occurs in the upper

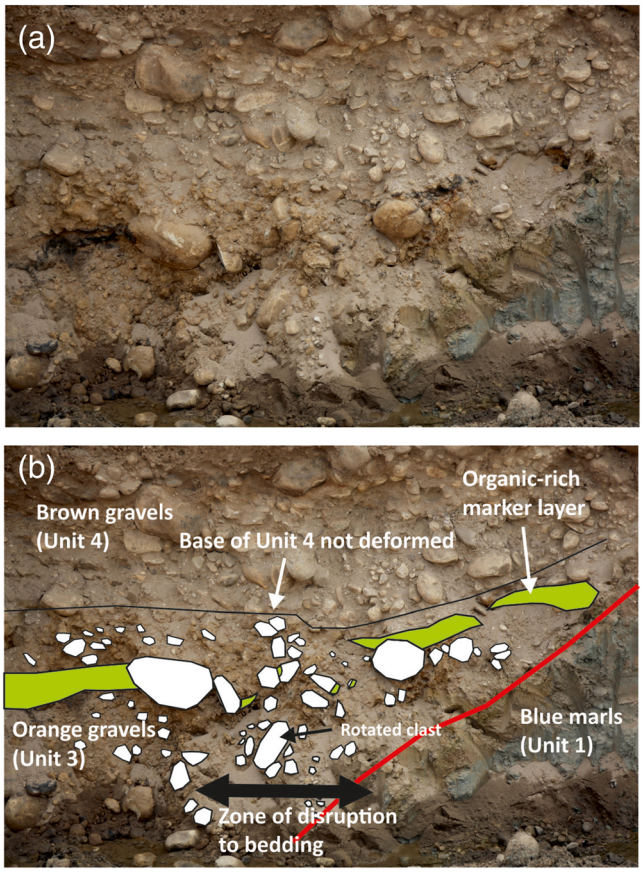

Figure 10. (a) Photograph of the base of the eastern quarry wall; see Figure 9b for location. (b) Interpretation, showing the main fault (F1) as a red line that separates pre-Holocene blue marls of Unit 1 from the Holocene gravels of the hanging wall. The basal part of the gravel sequence is represented by Unit 3. A dark organic-rich marker band within this unit, from which sample Weinan-3 with age 4800–4619 cal BCE was taken, is highlighted in green. The thick black arrow marks a zone of disruption within the Unit 3 bedding. Within this zone the dark marker band is fragmented and clasts are rotated, with some of these rotated clasts retaining organic-rich staining on their sides.

part of Unit 3_e and forms a marker layer that is continuous for at least 10-m horizontal extent within the hanging wall as exposed in the quarry. The organic-rich layer is continuous and undisturbed except for ~2 m from Fault F_{1e}, where we interpret an alignment of rotated clasts and disruption of the bedding as representing a diffuse fault zone ($F3_e$). The fault does not displace the contact between Unit 3_e and the overlying brown gravels (Unit 4_e). The slip therefore appears to have occurred between deposition of Units 3_e and 4_e and hence from an earlier event than the one that resulted in $F1_e$ and $F2_e$ (Figures 9 and 10).

Unit 4_e is composed of coarse brown gravels and is unconformable on the underlying Unit 3_e, with a distinct erosion contact (Figure 10). There is some indication of sedimentary structure within Unit 4_e, particularly in the presence of convex-down channel profiles in its lower part (green lines in Figure 9). The channels appear to have cut into an underlying finer gravel deposit, and the basal part of the channel infill is coarse, with the upper part being finer. These channels, and the underlying finer gravel unit, do not appear to be displaced by faulting or fissuring.

Unit 5_e does not possess the same extensive silt bands as seen on the western wall, though an overall reduction in maximum clast size is still apparent. One prominent, though localized, silt deposit is observed in the southernmost part of the hanging wall and is truncated at Fault $F2_e$. This silt deposit appears to have infilled a lens-shaped channel as described by Li et al. (2015), who made their observations after the quarry wall had moved eastward. Li et al. (2015) interpret the silt as infilling a hanging wall fissure and occurring after the most recent event. However, its truncation by $F2_e$ as visible in Figure 9 shows that it actually predates the most recent slip event. The silt-filled channel may indicate infilling of a fissure from an earlier earthquake, which was then deformed by the most recent event. Although the presence of a wide fissure would be consistent with the western quarry wall, the presence of several undeformed horizons at deeper levels within the stratigraphy (the black mud, finer gravel layer, and the base of the channels themselves) does not seem compatible with that idea, and we suggest instead that the hanging wall deformation is considerably different between the two quarry walls, with only a narrow sheared fault zone present in the eastern wall. However, given the coarse blocky hanging wall material, and the removal of the upper parts of the faulted units by the later erosion, it is possible that elements of hanging wall deformation have not been recognized and interpreted.

The faulted units are covered by a coarse gravel Unit 7_e, which has an irregular channelized base that has incised into older gravels in the footwall. The whole system is covered by a continuous silt layer (Unit 8_e), in which a thin layer of organic-rich rootlets is preserved in a paleosol. Unfortunately, we were unable to access the paleosol layer for sampling. The silt layers have been covered by fluvial gravels of Unit 9_e. The base of Unit 10_e has incised into Unit 8_e and truncates the paleosol marker horizon. The sharp erosive margins of Unit 10_e define a palaeo channel. Units 7_e and younger are not deformed across the fault and must postdate the earthquake. We note that grain size in Units 7–10 varies considerably between outcrops on the eastern and western walls, suggesting that postearthquake deposition was likely to be channelized and spatially variable.

4.3. Summary Trench Interpretation

In Figure 11 we present a reconstruction of the structural and stratigraphic development of the western trench wall, as shown in Figure 8. In the reconstruction we show the fissuring and subsequent infill forming due to a single surface rupturing earthquake, which is possible given the observations from the quarry

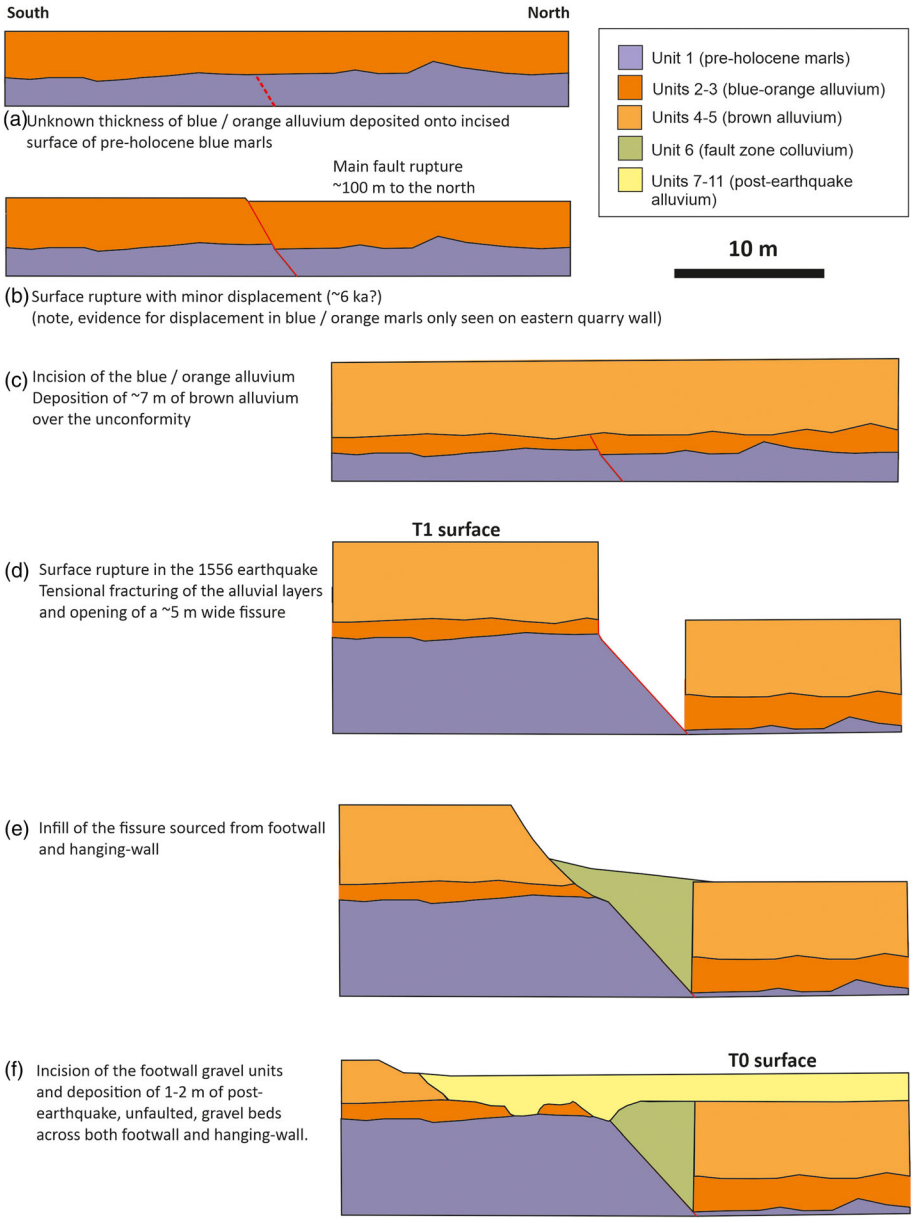

Figure 11. (a–f) Cartoons showing the structural and stratigraphic development of the exposures of the western quarry wall (cf. Figure 7). These cartoons assume that the fissure was developed and infilled in a single earthquake cycle. The exposed stratigraphy and structures do not allow us to exclude a multiple event origin.

wall, but not certain, and it is also possible that the fissure fill records more than one earthquake, as described earlier.

Blue and orange gravel layers (Units 2 and 3) were first laid down unconformably on the blue marls (Unit 1), which constitutes the oldest exposed sediment (Figure 11a). The gravels were then faulted (Figure 11b) but with only minor displacement. We have evidence for this surface rupture from the eastern quarry wall only but have shown it here on the western wall for illustrative purposes. From borehole constraints (introduced in section 4) we infer that greater surface slip occurred on a second fault strand sited north of the exposure. In Figure 11c we show deposition of gravels (Units 4 and 5), whose base incises into the underlying gravels and whose deposition postdates the first surface rupture. Units 4 and 5 are then faulted, fissured, and displaced vertically by ~7 m (Figure 11d). The measurement is the same whether from the base or the top of

Unit 4, indicating that the entire thickness of Unit 4 was laid down and then faulted in one or more events. The footwall constitutes the T1 surface observed in the geomorphology. The fissure was infilled by sediment from the immediate hanging wall and footwall (Figure 11e) and then the footwall sequence was incised, and ~2 m of postearthquake sediment was deposited (Figure 11f). The surface of these sediments constitutes the T0 surface, into which the active river channel is incised. We now go on to describe and discuss the available age control.

4.4. Age Constraints From the Trench

We took six samples from the western trench wall for radiocarbon dating and five from the eastern wall (Figure 7). The uppermost samples from the eastern wall were collected from a pit dug into the ground surface, as the quarry wall was unstable. We collected two types of samples: bulk ages of organic materials in the sediment (shown as green circles in Figure 7) and detrital charcoals (shown as yellow circles in Figure 7). In general there is a wide spread in ages extracted from the fluvial gravels exposed in the quarry walls, and the ages are not in stratigraphic order (Table 1). Given these observations, we suggest that the organic-rich "bulk" samples may be leached or may have absorbed older carbon components. We interpret scatter within the charcoal radiocarbon ages obtained from within the gravel deposits to result from predepositional inheritance and potentially also from reworking of sediment. As a consequence the radiocarbon ages do not unambiguously reflect the real deposition ages of the sediment.

The recent faulting took place after deposition of Units 4 and 5 and before deposition of Unit 7. Sample CGC-3 (charcoal), Weinan-4 (charcoal), and CGC-1 (organic clay) from silty beds in Unit 5 return ages of 901–1116 cal CE, 1211–1020 cal BCE, and 6215–6060 cal BCE. The same layer from the eastern wall returned an age of 6865 ± 80 years (see Li et al., 2015). Due to the wide dispersion in radiocarbon ages and because units should predate the last surface rupturing event, we therefore assume that the younger of those ages (901–1116 cal CE) most immediately predates the most recent earthquake.

We also collected samples from the unfaulted units in the uppermost parts of the exposed stratigraphy, whose deposition postdates the most recent surface faulting. We found large dispersion in radiocarbon ages ranging between 9235 cal BCE and 1222 cal CE. No subset of those ages is in a good stratigraphic order, reflecting the difficulty of constraining age of deposition using organic-rich materials. The only charred sample (CGC-4) yields an age of 1042–1222 cal CE. Radiocarbon ages obtained from shells in the unfaulted units by Li et al. (2015) yielded clustered ages of ~2.5–3.1 ka. From our morphological mapping, the ages of these unfaulted deposits are related to the T0 surface, which postdates the most recent surface rupture (see Figure 4b). The shell ages of Li et al. (2015) are not consistent with our 901–1116 cal CE predate for the most recent rupture, as described above.

In section 2 we showed that the two charcoal ages obtained from soils each overlying the gravel terrace deposits of T1 and T2 were clustered between themselves and, in the case of T2, yielded ages that were consistent with the timing of the Banpo culture, artifacts of which were found mixed in with the charcoal. We are therefore confident that charcoal from soils overlying the T1 and T2 gravel terraces has little inheritance and returns ages close to the depositional age of the surrounding sediment. Following this reasoning, the two charcoal samples (HX13-C7 and HX13-C8), which we collected from soils, overlying and hence postdating, the T1 alluvial gravels return ages of 392–206 cal BCE and hence provide a lower bound for the emplacement of the T0 level, as it must be younger than T1. This observation implies that the unfaulted units are consequently younger than this. The youngest sample age from the postfaulting deposits exposed in the quarry is CGC-4 with an age of 1042–1222 cal CE, though this sample is likely to also contain some inheritance.

From the available age constraints, we can only state that the most recent seismic event occurred since 901–1116 cal CE. It is unlikely that another earthquake of equivalent size to the 1556 event is missing from the historical records, which are thought to be complete to magnitude 6 from ~1300 CE and complete for larger earthquakes for ~2000 years (e.g., Liu et al., 2011). The event is thus very likely to be the 1556 Huaxian earthquake, as this is the only large event in this area in the historical records (e.g., Figure 1a).

There is evidence for at least one previous rupture in the eastern quarry wall, where an alignment of rotated clasts in the blue-orange gravels (Unit 3_e), at the base of the hanging wall sediments, defines a shear zone (Figure 10). Unit 3e is observed on both sides of the fault zone and on both quarry walls. On the footwall exposed in the western wall, we dated an organic-rich soil (Weinan-2) at the top of Unit 3_e at 4946–

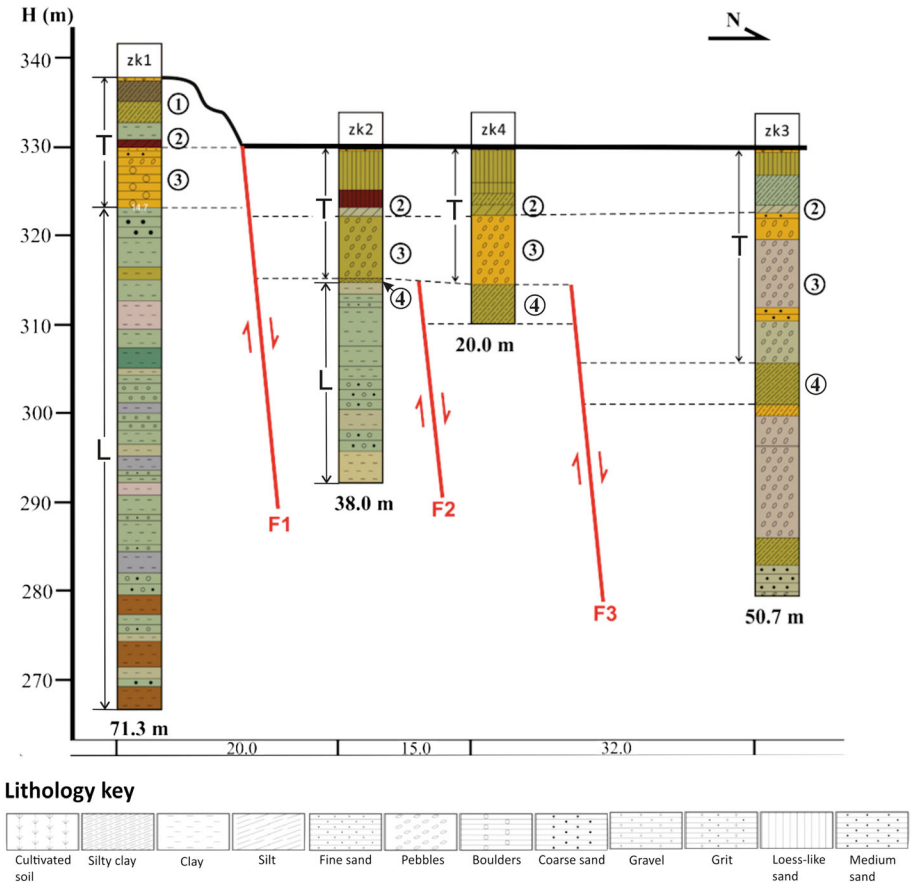

Figure 12. Borehole cross section at the Chishui site (see Figure 3 for location). Four boreholes (zk1-zk4) were drilled, with a depth of 71.3 m (zk1), 38.0 m (zk2), 20.0 m (zk4), and 50.7 m (zk3). Colors on the figure are representative of the color of each bed, and grain size is represented by ornamentation (see key at the base of the figure). We infer the presence of three fault splays (F1, F2, and F3) from changes in the stratigraphy between the four boreholes. In zk1 the deposits are divided into terrace gravels (T) and older lacustrine clays (L). The lacustrine deposits were not encountered in boreholes zk3 and zk4, which instead show a thickened and longer-lived sequence of coarser-grained sediments.

4787 cal BCE. On the hanging wall, ages of 4800–4619 cal BCE and 6235–6084 cal BCE are obtained for Weinan-3 (charcoal, eastern wall) and CGC-8 (organic clay, western wall), respectively. The erosional base of the overlying brown gravel layer (Unit 4_e) is not displaced (Figure 10). We have no direct age constraints on the lower part of Unit 4_e that would postdate the older event, and we can only say that this seismic event occurred after ~6.6 ka. As stated in the quarry wall interpretations, we cannot rule out the occurrence of an additional event, or events, between the most recent (likely 1556) earthquake and the post 6.6 ka event.

5. Borehole Cross Section

Four boreholes (zk1-zk4) with depths of 71.3 m (zk1), 38.0 m (zk2), 20.0 m (zk3), and 50.7 m (zk4), respectively, were drilled across the fault scarp at the western side of the Chishui river catchment (the borehole locations are marked as white circles in Figure 4b). Cores were extracted and stratigraphic logs compiled (Figure 12). We label some units to aid in correlation between the cores, but the numbering does not correspond to the units described in the quarry wall logs.

We infer the presence of three fault splays from correlation of the stratigraphy between the boreholes. F1 offsets the upper sediment layer made up of gravels and silt clays (Unit 1 in zk1 and Unit 2 in zk2) by 7–8 m, suggesting that the most recent rupture occurred on F1. The vertical offset at depth agrees well with the

7.5 m fault scarp in the T1 surface and in the ~7 m of vertical separation measured from the quarry exposures. The sequence of units below Unit 1 is predominantly lacustrine sediments, presumably the same deposits as seen in the quarry exposure (Figures 7–9). We did not find clear evidence for offset features on Fault F2, but the silt clay layer (Unit 4 in zk4) is much thicker than the same sediment in zk2 (Unit 4), which suggests that Unit 3 in zk2 was uplifted and has been eroded since then, whereas the same layer in zk4 in the hanging wall of F2 has been preserved. Above Unit 3, the gravel layer that was offset by F1 was not affected by F2 (i.e., Units 2 and 3 are continuous in zk2 and zk4), indicating that faulting on F2 was earlier than F1. The earliest rupture (F3) offsets Unit 4 between zk3 and zk4 by ~10 m.

The three fault splays show that the earthquake ruptures are not colocated along the borehole section line. Although we do not have any dates from the boreholes, the stratigraphy exposed in zk1 is very similar to the quarry exposure, with ~8-m-thick orange gravels overlying banded blue-gray muds and silts. The vertical offset is also similar (~7–8 m), suggesting that the event on Fault F1 is the most recent surface rupturing earthquake, as visible in the quarry walls. None of the individual fault splays shows sufficient throw to account for the ~14-m-high T2 scarp, suggesting that the T2 scarp may have been substantially modified, with two closely spaced scarps now amalgamated as one.

6. Palaeoseismic History

Analysis of the Pleiades DEM shows scarp heights of 7.5 and ~14 m (Figures 3 and 4). The lower scarp height is similar to the throw observed in the quarry walls for the top and base of Unit 4, such that topographic measurements of scarp height approximate to fault throw. The higher scarp, however, is likely to underestimate the throw over this longer time interval, as gravel units are interpreted to thicken in the hanging wall in the borehole profiles (Figure 12), and there is also evidence from the borehole profiles that the scarp has been modified significantly. The scarp in the central part of the Chishui catchment has been almost entirely removed by fluvial erosion after the most recent earthquake. The available age control on the displaced terraces T1 and T2 comes solely from the overlying soil layers, and hence, for both we may only determine a minimum age (terminus ante quem) for the cessation of fluvial deposition.

The fluvial gravels of the youngest displaced terrace (T1) had been removed from the active river system by ~2.2–2.4 thousand years ago, much earlier than the destructive 1556 earthquake, and yet the quarry exposure retains evidence for rupture over the last 900 years that we infer to be caused by the 1556 earthquake. This may mean that the T1 surface has been uplifted by more than one earthquake over the last few thousand years. However, the ages can also be explained by a single earthquake if the development of T1 and T2 occurred in a similar manner to that seen for the youngest, postearthquake, terrace (T0). In this scenario, an initial aggradation of river gravel within the Chishui catchment, potentially at the last glacial-interglacial transition (e.g., Rost, 2000), was followed by downcutting of the active channel (Figure 13a). The highest observed terrace (T3) may represent remnants of the original postglacial surface that was dissected by river downcutting in a similar manner to how the postearthquake Terrace T0 has been channelized and incised following initial aggradation. Terraces T2 and T3 were offset vertically in the penultimate earthquake, or earthquakes, and then abandoned (Figure 13b). A radiocarbon age from faulted orange gravels (Unit 3_e) constrains the event that caused initial displacement of the T2 and T3 terraces to after ~6.6 ka, which is likely to predate the thick soil development (3988–3785 cal BCE) with the Banpo cultural objects that is found on top of the T2 and T3 surfaces.

Meanwhile, downcutting of the active channel removed most of T2 and T3 on its western margin. Initial aggradation of sediment followed by incision led to the formation of Terrace T1. Farming and soil development started on T1 since it was removed from the active river system by channel entrenchment before 392–206 cal BCE (Figure 13c).

Terrace T1 was subsequently displaced, either by a single or by multiple earthquakes. In Figure 13d we show an interpretation of displacement in a single earthquake. In this scenario the 1556 Huaxian earthquake offset Terrace T1 increased the offset of T2 and T3 and was accompanied by widespread landsliding upstream (Figure 13d). The rupture from this most recent event appears not to be colocated with that of earlier events in the western part of the study area, as the boreholes exposed three fault splays, ~65 m apart, and the quarry exposure appears to show only minor displacement of the orange gravels by what we interpret as the fault responsible for initial displacement of the T2 and T3 terraces. However, in the eastern part of the study

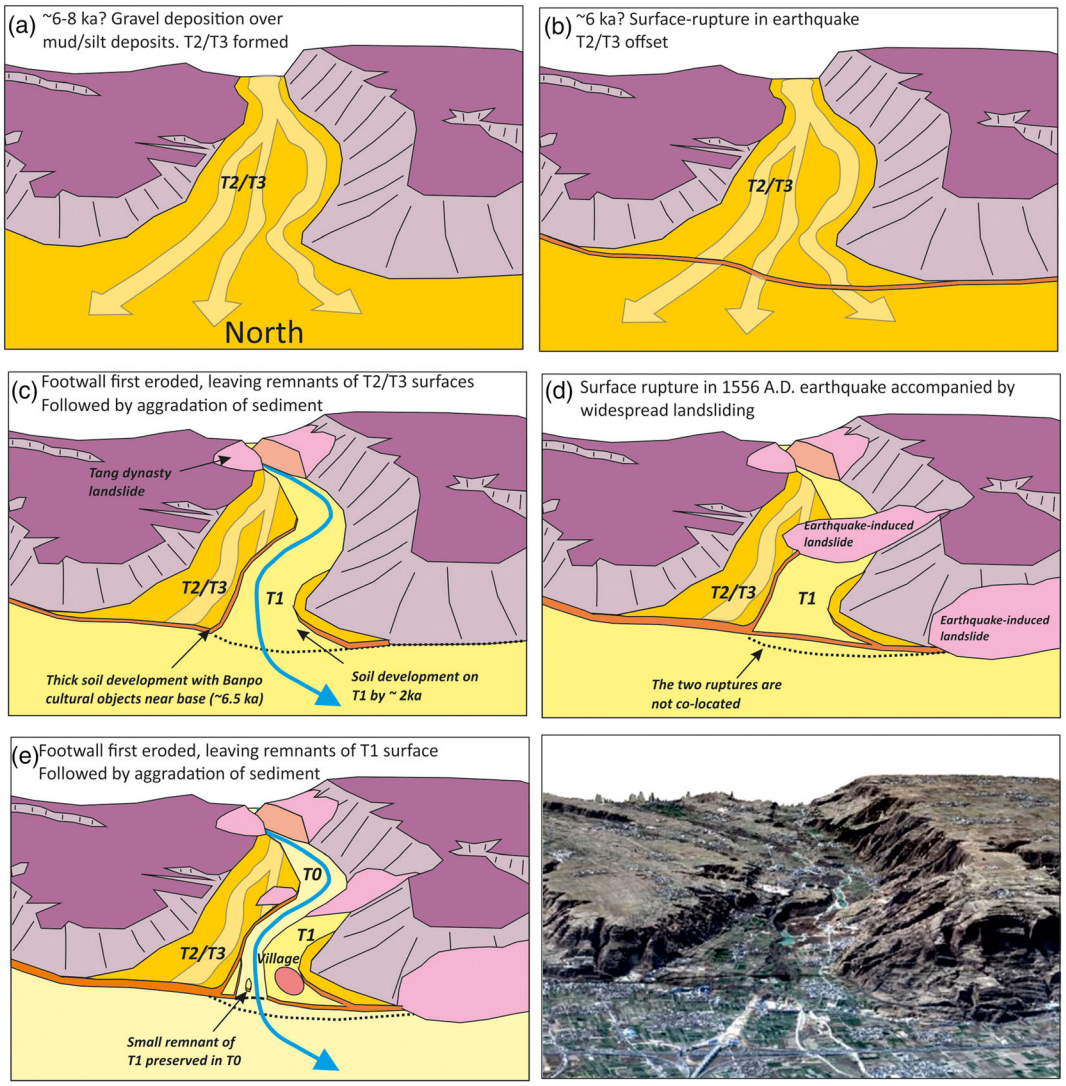

Figure 13. Cartoons showing the landscape evolution of the Chishui river catchment. (a) T2/T3 started to form. (b) Penultimate earthquake offsets T2/T3. (c) Footwall was eroded, leaving remnants of T2/T3 surfaces followed by aggradation of sediment. (d) Surface rupture in the 1556 Huaxian earthquake, causing widespread landsliding. (e) Footwall was eroded. (f) The 3-D perspective view of the present-day land surface.

area, the development of a 14-m scarp in T2 indicates rupture along a single trace in at least two earthquakes. Since the 1556 earthquake, the footwall was eroded, leaving remnants of T1, followed by aggradation of sediment to form T0, which was then also incised by the presently active channel (Figure 13e). Evidence of landslides and remnants of the preserved T1 surface in T0 are visible in the present-day imagery (Figure 13f).

7. Magnitude Estimate for the 1556 Earthquake

We consider the upper bounds on all the fault parameters in order to estimate the likely maximum magnitude for the 1556 earthquake. Having demonstrated that the Weinan fault is likely to have slipped in the 1556 earthquake, we presume, despite the previous objections (Hou et al., 1998; Li et al., 2015; Wang, 1980), that the neighboring Huashan fault slipped also (as is suggested by both by the presence of scarps along that segment and by the observed distribution of ground shaking). This assumption gives an upper bound of ~90 km on the combined length of the causative faults (Figure 2). Microseismic data in the Weihe graben show a seismogenic thickness of ~20 km (Yuan & Feng, 2010); given the large slip in

this earthquake, we consider that rupture may have extended to greater depths than the modern microearthquakes, allowing a maximum depth of 30 km. We assume that the dip at the surface, measured at 45°N in the quarry exposure, is representative of the slip at depth.

We measured 10-m slip from the quarry exposures, which is also consistent with the ~7.5-m scarp on which Chishui village sits. Scarps of up to this height are also observed along parts of the Huashan fault. It is possible that the scarps formed in a single earthquake, though multiple earthquake intepretations cannot be excluded. We therefore take 10 m to be the maximum slip for magnitude calculations. Given an absence of systematic measurements of scarp height along the Weinan and Huaxian faults, it is difficult to estimate the average slip assuming a single earthquake or for the most recent slip if the scarp has arisen in more than one earthquake. Nonetheless, the measurement of 10 m is likely to capture the maximum possible magnitude of the 1556 earthquake, from which we can compare to the magnitudes estimated from seismic intensities.

The seismic moment M_0 is the product of the modulus of rigidity of the rocks in which the fault is embedded, with the area of the fault that slipped in the earthquake and the slip in the earthquake. We use a shear modulus of 33 GPa and approximate the fault as being a rectangle of length 90 km and down-dip width 30/sin (45°) km. We repeat the calculation for different amounts of slip, with 10 m as the largest value used. These quantities, which are at the upper end of the range of the relevant observations, give an estimate of the seismic moment of 1.3×10^{21} N m with slip of 10 m, which corresponds to a moment magnitude of 8.0 (Hanks & Kanamori, 1979). If an estimate of 8 m is accepted for the average slip, the magnitude reduces to 7.9, and if the average slip is 5 or 3 m, the moment magnitude is further reduced to 7.8 or 7.6. If, additionally, the maximum depth of slip were 20 km (it is unlikely to have been less than this, given modern microseismicity) then the moment, assuming 8-m average slip, reduces to 6.7×10^{20} N m, which corresponds to a moment magnitude of 7.8 or to 7.7 if the average slip is 5 m or 7.5 if the average slip is 3 m.

The previously proposed magnitude of 8¼–8½ would require the seismic moment to have been between 2.4×10^{21} and 5.6×10^{21} N m. Even if we use our maximum estimate of slip, which itself may significantly overestimate the true magnitude, this value would still require that our estimate of the fault area is too small by a factor of between 2 and 10. We consider that to be improbable and therefore conclude that the previously proposed magnitude range of 8¼–8½ overestimates the moment of the 1556 Huaxian earthquake. Although we can demonstrate that the magnitude of the Huaxian earthquake was substantially smaller than previously proposed, the geological observations presented here are too limited to directly estimate the magnitude with any degree of certainty.

Scarps along the Weinan and Huashan faults have heights of up to 7–8 m on both segments, which suggests that the 1556 earthquake involved relatively large amounts of slip. The maximum throw of 7–8 m is larger than for other major historical normal faulting earthquakes in central China, which had similar rupture lengths but smaller peak displacements (e.g., Middleton et al., 2016; Xu et al., 2018). However, the existing measurements of scarp height along the Huaxian rupture suggest substantial variability along strike, and we also cannot exclude the possibility that the 7–8 m scarps formed in more than one earthquake. It is possible therefore that the Huaxian earthquake was comparable still comparable in magnitude to the other historical normal faulting earthquakes in central China.

In comparison to more recent global examples of large normal faulting earthquakes, we can say that the Huaxian earthquake is comparable or larger than the 1887 Sonora, Mexico, earthquake which had a total length of just over 100 km and a peak slip of ~2.7 m (Suter, 2008; Suter & Contreras, 2002). It was likely larger than the 1915 M_w ~ 7.0 Pleasant Valley, Nevada, earthquake, which had average throw of 2 m over a 59-km rupture length (Doser, 1988; Page, 1935); the 1957 M_w 7.1 Muya, Siberia, earthquake (e.g., Doser, 1991; Emmerson et al., 2006), which generated surface slip of ~4 m over a distance of 35 km (Molnar & Deng, 1984); and the 1959 M_w 7.2 Hebgen Lake earthquake, Montana, which had a mean throw of 3.6 m on a 36-km fault (e.g., Johnson et al., 2018).

The maximum magnitude of normal faulting earthquakes is often believed to be constrained by the lengths of fault segments, which in turn are thought to scale with the thickness of that portion of the crust which can support long-term stresses elastically (e.g., Jackson & White, 1989; Wallace, 1989). Under this view, the exceptional length and offset in a prehistoric earthquake inferred on the Bilila-Mtakatake fault can be

attributed to the exceptional elastic thickness of the region (Jackson & Blenkinsop, 1997). Alternatively, an exceptionally large normal faulting earthquake might be caused by the simultaneous rupture of several discrete segments along a fault that normally fails in smaller earthquakes along individual segments. Neither of these explanations is likely to apply to the Huaxian earthquake; the seismogenic thickness is not abnormally large for a continental interior setting, and the individual fault segments are not abnormally long (approximately 30 km; see Figure 2). Equally, a maximum slip of ~10 m, already large for a fault of length 90 km, would be unprecedented for rupture of an individual fault segment of 30 km. We suggest that the Huashan-Weinan faults may, therefore, belong to a group of faults that fail in earthquakes with high slip to length ratio (on the order of 10 cm/km in length). This class of faults is typically found within slow strain rate regions and may correlate with structural maturity of the faults (Hecker et al., 2010). Examples of this class of fault rupture include the 1959 Hebgen Lake, Montana, and 2014 Yutian, Tibet, earthquakes (e.g., Elliott et al., 2010; Johnson et al., 2018) and the proposed prehistoric Egiin Davaa event in Mongolia (e.g., Walker et al., 2017).

8. Implications for Seismic Hazard in the Weihe Basin

The Huashan and Weinan faults, on which the Huaxian earthquake took place, occupy approximately one quarter of the length of a system of faults that run for approximately 400 km along the southern margin of the Weihe Basin (see Figure 1b). These faults are generally coincident with the steep range front of the Qinling mountains, and it is therefore prudent to consider that other parts of the faults system may be capable of hosting large earthquakes such as in 1556. For example, a historically documented earthquake around 780 BCE may have ruptured the North Qinling fault at the southern margin of the Weihe graben, but little is known about this event, and the attribution of a causative fault remains uncertain (e.g., Feng et al., 2015).

We do not have enough information on the Huashan and Weinan faults to determine a recurrence interval or indeed whether that concept is appropriate here. If the two scarps at the Chishui site are developed in only two earthquakes, there is an interval of approximately 5,000 years between the 1556 Huaxian earthquake and its predecessor. If this interval was to prove typical of this and other faults on the southern margin of the Weihe Basin, then one such earthquake might be expected, somewhere along that margin, approximately once per thousand years. If instead the scarps are composite features resulting from multiple earthquakes, then the recurrence interval would be shorter. However, while the 1556 earthquake attracts much attention because of its enormity, concentration on such large-to-great earthquakes distracts attention from the risks posed by smaller, more frequent earthquakes in the Weihe Basin, where millions of people reside in rural dwellings that are vulnerable to earthquakes of magnitude as low as 6.

Two principal considerations apply in this regard. First, supposing the Huaxian earthquake had a moment magnitude of 7.9, at the upper end of the magnitude range we have estimated, and that earthquakes in the basin follow the Gutenberg-Richter relation between magnitude and frequency (Gutenberg & Richter, 1954), then a magnitude 7 earthquake in the basin is to be expected approximately every 500 years and a magnitude 6 earthquake every 50 years. Although the historical record is sure to be incomplete, such information as has been collected (State Seismological Bureau, 1995) is consistent with this approximate estimate. Second, those magnitude 6 and 7 earthquakes were not confined to the range-bounding faults but took place throughout the Weihe Basin on smaller faults that often are concealed by the effects of continuing deposition of sediments and by agricultural degradation of fault scarps. For instance, the 25 May 1568 CE, Gaoling, Sha'anxi, earthquake has a mesoseismal area that is focused in a linear region within the basin (State Seismology Bureau, 1986). The uncertainties in recurrence intervals on the major faults of the region and in the locations of minor faults that may nevertheless host earthquakes capable of causing significant loss of life render probabilistic estimate of risk significantly more uncertain than in regions, such as California or Japan, where the locations of dangerous faults, the likely maximum magnitudes of earthquakes upon them, and even the recurrence intervals, are reasonably well known.

9. Conclusions

Detailed analysis of the high-resolution DEM of the surface geomorphology at the Chishui river catchment, along with a recent fault exposure in a nearby quarry excavation and borehole cross section, allows us to

conclude that Weinan fault ruptured in an earthquake within the last ~1,000 years. Although we cannot be certain, the absence of other potential sources of an earthquake this size in the historical record indicates that this earthquake was the 1556 Huaxian event. The evidence presented from the Chishui site is compatible with a single earthquake involving throw of 7–8 m at this site, though we cannot exclude that this throw developed due to multiple smaller earthquakes. The magnitude of the Huaxian earthquake remains uncertain, but we can assign an upper limit, assuming it broke both the Weinan and Huashan faults, of M_w 8.0, with the actual value anywhere in the range down to M_w 7.5. These values are smaller than the previously inferred range of 8¼–8½, based on historical records of shaking and damage.

This study of the 1556 earthquake in the Weihe graben demonstrates the importance of combining modern high-resolution imagery, digital topographic models, and geological data to reexamine past earthquakes. The landscape in this part of the world is modified continually by both human and natural effects and as a result it is sometimes difficult and often impossible to delineate the extent and slip of surface ruptures. Identification and documentation of active faulting are increasingly urgent for the assessment of earthquake hazard, especially given that rapid urban development in recent decades can erase the evidence of fault activity (e.g., fault scarps and uplifted river terraces) within years or even a few days. For example, a few weeks after our fieldwork, the trench structures we report here were destroyed by roadworks. Our structure-from-motion model preserves the site, showing the usefulness of the technique for digital preservation, while our Pleiades DEM preserves the shape of the terraces prior to quarrying. It is increasingly pressing to work on such regions in order to quantify and archive the historical seismic activity of regions where millions of people live. Palaeoseismological and geomorphological studies are needed to investigate this fault (as well as other faults in the Weihe Basin) in the future.

Appendix A: Details of Satellite Image Acquisition and Digital Elevation Model Extraction

Pleiades stereo imagery (0.5-m resolution) was acquired on 30 December 2013 by Pleiades 1A, with a stereo angle of 30°. Global Positioning Systems (GPS) measurements were collected in the field using the network Real Time Kinematics (RTK) from the CEA Shaanxi Province to calibrate and evaluate the Pleiades DEM. Pleiades data were processed using the Leica Photogrammetry Suite (LPS). The 28 tie points and 2 GPS measurements taken from crossroads were used to refine the original rational function model (RFM). After refining the RFM, a pixel-by-pixel matching procedure was implemented, with a relatively small window size of 5×5 pixels to avoid strong smoothing of the topographic surface. The resulting point cloud from the pixel-by-pixel matching was filtered by averaging within a block of 1 m and then gridded with a pixel spacing of 1 m (WGS84 UTM 49N) using the continuous curvature splines in tension. Compared to the RTK measurements, the resulting Pleiades DEM has an error of -0.1 ± 0.3, -0.4 ± 0.5, and -0.5 ± 0.3 m in X, Y, and Z directions, respectively.

Acknowledgments

This work was funded by the Natural Environment Research Council and the Economic and Social Research Council of the UK, under Grant NE/J02001X/1 (Earthquakes without Frontiers), by a joint programme between NERC, ESRC, and the National Natural Science Foundation of China, under Grants NE/N012313/1 and NE/N01233X/1, and by NERC through its support for its Centre for the Observation and Modelling of Earthquakes, Volcanoes, and Tectonics. We also thank the Leverhulme trust for support through the EROICA Project RPG-2018-371. We thank Alexandra Hatem, David Schwartz, an anonymous reviewer, and the Editors for thoughtful reviews that helped to sharpen the interpretations and shape the overall paper.

Data Availability Statement

FAIR data access statement: The Pleiades stereo satellite imagery used to construct the digital elevation model of the Chishui site is archived and available for purchase from the imagery provider (AIRBUS Defense and Space; https://www.intelligence-airbusds.com/geostore/).

References

Bureau, S. S. (1986). *Atlas of historical earthquakes, Ming Dynasty*. Beijing: China Cartographic Publishing House.

Dai, W., & Feng, X. (2004). Lateral migration of fault activity in Weihe basin. *Acta Seismologica Sinica*, *17*, 190–199. https://doi.org/10.1007/BF02896933

Doser, D. I. (1988). Source parameters of earthquakes in the Nevada seismic zone, 1915–1943. *Journal of Geophysical Research*, *93*(B12), 15,001–15,015. https://doi.org/10.1029/JB093iB12p15001

Doser, D. I. (1991). Faulting within the eastern Baikal rift as characterized by earthquake studies. *Tectonophysics*, *196*(1–2), 109–139. https://doi.org/10.1016/0040-1951(91)90292-Z

Du, J., Li, D., Wang, Y., & Ma, Y. (2017). Late quaternary activity of the Huashan Piedmont fault and associated hazards in the southeastern Weihe Graben, Central China. *Acta Geologica Sinica (English Edition)*, *91*(1), 76–92. https://doi.org/10.1111/1755-6724.13064

Elliott, J. R., Walters, R. J., England, P. C., Jackson, J. A., Li, Z., & Parsons, B. (2010). Extension on the Tibetan plateau: Recent normal faulting measured by InSAR and body wave seismology. *Geophysical Journal International*, *183*(2), 503–535. https://doi.org/10.1111/j.1365-246X.2010.04754.x

Emmerson, B., Jackson, J., McKenzie, D., & Priestley, K. (2006). Seismicity, structure and rheology of the lithosphere in the Lake Baikal region. *Geophysical Journal International*, *167*(3), 1233–1272. https://doi.org/10.1111/j.1365-246X.2006.03075.x

Farr, T. G., & Kobrick, M. (2000). Shuttle Radar Topography Mission produces a wealth of data. *Eos, Transactions American Geophysical Union*, *81*(48), 583–585.

Feng, X., Walker, R., & England, P. (2015). Current knowledge on seismic hazards in Shaanxi province. In *Pathways to earthquake resilience in China*. London, U.K: Report of the Overseas Development Institute.

Gutenberg, B., & Richter, C. F. (1954). *Seismicity of the Earth and associated phenomena*. Princeton, New Jersey: Princeton University Press.

Hanks, T. C., & Kanamori, H. (1979). A moment magnitude scale. *Journal of Geophysical Research*, *84*(B5), 2348–2350. https://doi.org/10.1029/JB084iB05p02348

Hecker, S., Dawson, T. E., & Schwartz, D. P. (2010). Normal-faulting slip maxima and stress-drop variability: A geological perspective. *Bulletin of the Seismological Society of America*, *100*(6), 3130–3147. https://doi.org/10.1785/0120090356

Historical Natural Disaster in Shaanxi Province Editorial Union (2002). *Historical natural disasters in Shaanxi province*. Beijing: China Meteorological Press.

Hou, J. J., Han, M. K., Chai, B. L., & Han, H. Y. (1998). Geomorphological observations of active faults in the epicentral region of the Huaxian large earthquake in 1556 in Shaanxi Province, China. *Journal of Structural Geology*, *20*(5), 549–557. https://doi.org/10.1016/S0191-8141(97)00112-0

Jackson, J., & Blenkinsop, T. (1997). The Bilila-Mtakataka fault in Malaŵi: An active, 100-km long, normal fault segment in thick seismogenic crust. *Tectonics*, *16*(1), 137–150. https://doi.org/10.1029/96TC02494

Jackson, J. A., & White, N. J. (1989). Normal faulting in the upper continental crust: observations from regions of active extension. *Journal of Structural Geology*, *11*(1-2), 15–36.

Johnson, K., Nissen, E., Saripalli, S., Arrowsmith, J. R., McGarey, P., Scharer, K., et al. (2014). Rapid mapping of ultrafine fault zone topography with structure from motion. *Geosphere*, *10*(5), 969–986. https://doi.org/10.1130/GES01017.1

Johnson, K. L., Nissen, E., & Lajoie, L. (2018). Surface rupture morphology and vertical slip distribution of the 1959 M w 7.2 Hebgen Lake (Montana) earthquake from airborne lidar topography. *Journal of Geophysical Research: Solid Earth*, *123*, 8229–8248. https://doi.org/10.1029/2017JB015039

Kaizuka, S., & Matsuda, T. (1992). Active faults in the Weihe basin and ground fissures in Xi'an City, Shaanxi Province. In *China—A report on the Janpan-China cooperative studies on earthquake prediction (1987–1989)*.

Kulikova, G., & Krüger, F. (2017). Historical seismogram reproductions for the source parameters determination of the 1902, Atushi (Kashgar) earthquake. *Journal of Seismology*, *21*(6), 1577–1597. https://doi.org/10.1007/s10950-017-9683-z

Lee, W. H. K., Wu, F. T., & Wang, S. C. (1978). A catalog of instrumentally determined earthquakes in China (magnitude greater than 6) compiled from various sources. *Bulletin of the Seismological Society of America*, *68*(2), 383–398.

Leonard, M. (2010). Earthquake fault scaling: Self-consistent relating of rupture length, width, average displacement, and moment release. *Bulletin of the Seismological Society of America*, *100*(5A), 1971–1988. https://doi.org/10.1785/0120090189

Li, D., Du, J., Ma, Y., & Xiao, A. (2015). Active faults and dip slip rates along the northern margins of the Huashan Mountain and Weinan loess tableland in the southeastern Weihe Graben, central China. *Journal of Asian Earth Sciences*, *114*, 266–278. https://doi.org/10.1016/j.jseaes.2015.08.013

Liu, M., Stein, S., & Wang, H. (2011). 2000 years of migrating earthquakes in North China: How earthquakes in midcontinents differ from those at plate boundaries. *Lithosphere*, *3*(2), 128–132. https://doi.org/10.1130/L129.1

Mackenzie, D., Elliott, J. R., Altunel, E., Walker, R. T., Kurban, Y. C., Schwenninger, J. L., & Parsons, B. (2016). Seismotectonics and rupture process of the MW 7.1 2011 Van reverse-faulting earthquake, eastern Turkey, and implications for hazard in regions of distributed shortening. *Geophysical Journal International*, *206*(1), 501–524. https://doi.org/10.1093/gji/ggw158

Middleton, T. A., Walker, R. T., Parsons, B., Lei, Q., Zhou, Y., & Ren, Z. (2016). A major, intraplate, normal-faulting earthquake: The 1739 Yinchuan event in northern China. *Journal of Geophysical Research: Solid Earth*, *121*, 293–320. https://doi.org/10.1002/2015JB012355

Molnar, P., & Deng, Q. (1984). Faulting associated with large earthquakes and the average rate of deformation in central and eastern Asia. *Journal of Geophysical Research*, *89*(B7), 6203–6227. https://doi.org/10.1029/JB089iB07p06203

Ou, Q., Yu, J., Kulikova, G., Parsons, B., & Walker, R. T. (2018). *Magnitude of the 1920 Haiyuan (China) earthquake re-estimated using a combined geological and seismological approach* (Vol. 2018, pp. S41D-0577). Washington, DC: AGU Fall Meeting Abstracts.

Page, B. M. (1935). Basin-range faulting of 1915 in Pleasant Valley, Nevada. *The Journal of Geology*, *43*(7), 690–707. https://doi.org/10.1086/624362

Rao, G., Lin, A., Yan, B., Jia, D., & Wu, X. (2014). Tectonic activity and structural features of active intracontinental normal faults in the Weihe Graben, central China. *Tectonophysics*, *636*, 270–285. https://doi.org/10.1016/j.tecto.2014.08.019

Rost, K. T. (2000). Pleistocene paleoenvironmental changes in the high mountain ranges of central China and adjacent regions. *Quaternary International*, *65*, 147–160. https://doi.org/10.1016/S1040-6182(99)00041-5

State seismological Bureau of China (1988). *Active faults along the margins of the ordos block (in Chinese)*. Beijing: Seismological press.

State Seismology Bureau of China (1995). *Atlas of the historical strong earthquakes in China (23rd century BC to 1911 AD)*. Beijing: Seismological Press.

Suter, M. (2008). Structural configuration of the Otates fault (southern Basin-and-Range Province) and its rupture in the 3 May 1887 M = 7.5 Sonora, Mexico earthquake. *Bulletin of the Seismological Society of America*, *98*, 2879–2893. https://doi.org/10.1785/0120080129

Suter, M., & Contreras, J. (2002). Active tectonics of northeastern Sonora, Mexico (southern Basin and Range Province) and the 3 May 1887 Mw 7.4 earthquake. *Bulletin of the Seismological Society of America*, *92*, 581–589. https://doi.org/10.1785/0120000220

Walker, R. T., Wegmann, K. W., Bayasgalan, A., Carson, R. J., Elliott, J., Fox, M., et al. (2017). The Egiin Davaa prehistoric rupture, central Mongolia: A large magnitude normal faulting earthquake on a reactivated fault with little cumulative slip located in a slowly deforming intraplate setting. *Geological Society, London, Special Publications*, *432*(1), 187–212. https://doi.org/10.1144/SP432.4

Wallace, R. E. (1989). Fault plane segmentation in brittle crust and anisotropy in loading systems. In D. P. Schwartz, & R. H. Sibson (Eds.), *Fault segmentation and controls on rupture initiation and termination. US geological survey open-file report 89* (Vol. 315, pp. 400–408). USA: United States Geological Survey.

Wang, J. (1980). Ground ruptures during the large earthquake of 1556, Huaxian County, Shanxi. *Acta Seismologica Sinica*, *2*(4), 430–437.

Wang, J.-M. (1987). The Fenwei rift and its recent periodic activity. *Tectonophysics*, *133*(3), 257–275. https://doi.org/10.1016/0040-1951(87)90269-1

Wells, D. L., & Coppersmith, K. J. (1994). New empirical relationships among magnitude, rupture length, rupture width, rupture area, and surface displacement. *Bulletin of the Seismological Society of America*, *84*(4), 974–1002.

Wesnousky, S. G. (2008). Displacement and geometrical characteristics of earthquake surface ruptures: Issues and implications for seismic-hazard analysis and the process of earthquake rupture. *Bulletin of the Seismological Society of America*, *98*(4), 1609–1632. https://doi.org/10.1785/0120070111

Westoby, M. J., Brasington, J., Glasser, N. F., Hambrey, M. J., & Reynolds, J. M. (2012). Structure-from-motion photogrammetry: A low-cost, effective tool for geoscience applications. *Geomorphology*, *179*, 300–314. https://doi.org/10.1016/j.geomorph.2012.08.021

Xu, Y., He, H., Deng, Q., Allen, M. B., Sun, H., & Bi, L. (2018). The AD 1303 Hongdong earthquake and the Huoshan Piedmont Fault, Shanxi Graben: Implications for magnitude limits of normal fault earthquakes. *Journal of Geophysical Research: Solid Earth*, *123*, 3098–3121. https://doi.org/10.1002/2017JB014928

Yanping, Z. (2013). The Early Neolithic in the central Yellow River valley, c. 7000–4000 BC. In *A companion to Chinese archaeology* (pp. 169–193). Oxford, UK: Blackwell.

Yuan, T., & Feng, X. (2010). *The 1556 Huaxian great earthquake* (p. 386). Beijing: Seismol. Press.

Zhang, A., Yang, Z., Zhong, J., & Mi, F. (1995). Characteristics of late Quaternary activity along the southern border fault zone of Weihe graben basin. *Quaternary International*, *25*, 25–31. https://doi.org/10.1016/1040-6182(94)P3715-K